Monthly Notices of the ROYAL ASTRONOMICAL SOCIETY

MNRAS **543,** 2633–2648 (2025) https://doi.org/10.1093/mnras/staf1545
Advance Access publication 2025 September 30

The broad-band view of the bare Seyfert PG 1426+015: relativistic reflection, the soft excess, and the importance of oxygen

D. J. Walton [1]★ A. Madathil-Pottayil,[1] P. Kosec,[2,3] J. Jiang,[4] J. Garcia,[5] A. C. Fabian [6] C. Pinto,[7] D. J. K. Buisson,[8] M. L. Parker [9] W. N. Alston [1] and C. S. Reynolds [10,11]

[1]*Centre for Astrophysics Research, University of Hertfordshire, College Lane, Hatfield AL10 9AB, UK*
[2]*MIT Kavli Institute for Astrophysics and Space Research, Massachusetts Institute of Technology, Cambridge, MA 02139, USA*
[3]*Center for Astrophysics | Harvard, Smithsonian, Cambridge, MA 02138, USA*
[4]*Department of Physics, University of Warwick, Gibbet Hill Road, Coventry CV4 7AL, UK*
[5]*NASA Goddard Space Flight Center, Greenbelt, MD 20771, USA*
[6]*Institute of Astronomy, University of Cambridge, Madingley Road, Cambridge CB3 0HA, UK*
[7]*INAF - IASF Palermo, via Ugo La Malfa 153, I-90146 Palermo, Italy*
[8]*Independent Researcher*
[9]*Optibrium Limited, Cambridge Innovation Park, Cambridge CB25 9GL, UK*
[10]*Department of Astronomy, University of Maryland, College Park, MD 20742-2421, USA*
[11]*Joint Space-Science Institute, College Park, MD 20742-2421, USA*

Accepted 2025 September 10. Received 2025 August 29; in original form 2025 July 14

ABSTRACT

We present results from a deep, coordinated *XMM–Newton* + *NuSTAR* observation of the type 1 Seyfert PG 1426+015, a source of particular interest as the most massive reverberation-mapped black hole to date ($\log[M_{\rm BH}/M_{\odot}] = 9.01^{+0.11}_{-0.16}$). The high-resolution RGS data confirm the 'bare' nature of the source, showing no evidence for absorption beyond the Galactic column, while the broad-band spectrum unambiguously reveals the presence of relativistic reflection from the innermost accretion disc (in the form of a relativistically broadened iron emission and associated Compton reflection hump) as well as confirming the presence of the strong soft excess reported previously. We explore whether relativistic reflection can successfully account for the soft excess along with the higher-energy reflection features, utilizing the two most-commonly used reflection codes (REFLIONX, XILLVER). Ultimately, we find that both models are able to successfully reproduce the soft excess, though in the case of the XILLVER model this is contingent on reducing the strength of the O VIII line included in the model, as otherwise this feature prevents the model from reproducing the data. The reflection models that successfully reproduce the broad-band data imply a relatively high density for the accretion disc of $\log[n_{\rm e}/{\rm cm}^{-3}] \sim 18$, consistent with the loose anti-correlation seen from other active galactic nuclie (AGNs) in the $\log[n_{\rm e}/{\rm cm}^{-3}]$ versus $\log[m_{\rm BH}\dot{m}^2]$ plane, as well as a moderate-to-high black hole spin of $a^* \gtrsim 0.7$. This preliminary spin constraint is strongly dependent on the assumption that the soft excess is dominated by relativistic reflection.

Key words: black hole physics – galaxies: active – X-rays: individual: (PG 1426+015).

1 INTRODUCTION

The reflected emission from the accretion disc provides one of our primary observational tools for probing the innermost regions around actively accreting black holes, particularly in the case of the supermassive black holes (SMBHs) powering active galactic nuclei (where the thermal emission from the disc typically emerges in the UV band, which is difficult to access owing to interstellar absorption). This arises as a natural consequence of the disc–corona geometry exhibited by these systems (as some of the hard X-ray emission from the corona must irradiate the surface of the optically thick accretion disc), and carries key information about the innermost radius of the accretion disc (*e.g.* Brenneman & Reynolds 2006; Dauser et al. 2010) as well as the geometry of the corona (*e.g.* Martocchia et al. 2000; Vaughan et al. 2004; Wilkins & Fabian 2012; Gonzalez et al. 2017). The former can in turn provide information about the spin of the black hole (Bardeen et al. 1972). This is a property that is of particular interest for SMBHs, as the growth history of these objects dictates their distribution in the spin–mass plane (*e.g.* Sesana et al. 2014; Bustamante & Springel 2019; Beckmann et al. 2024). A growing number of reflection-based SMBH spin constraints are available in the literature (∼40–50 to date; see Reynolds 2021; Bambi et al. 2021 for recent reviews). These are mostly limited to relatively low mass black holes ($M_{\rm BH} \lesssim 10^8\,{\rm M}_{\odot}$), but spin measurements for the largest black holes are of particular importance for constraining SMBH growth models (Piotrowska et al. 2024).

★ E-mail: d.walton4@herts.ac.uk

The reflected emission is dominated by a series of fluorescent emission lines, among which the iron line at ∼6.4–7.0 keV (depending on ionization state) is typically the strongest, along with a characteristic high energy continuum that peaks at ∼30 keV and is often referred to as the 'Compton hump' (*e.g.* George & Fabian 1991; Ross & Fabian 2005; García & Kallman 2010). While the emission lines are narrow in the rest frame of the disc, to an external observer they will be subject to the relativistic effects associated with the orbital motion and the strong gravity close to a black hole, resulting in a broadened and skewed 'discline' profile (*e.g.* Fabian et al. 1989; Laor 1991); the detailed form of this profile is determined by the combined disc–corona geometry. As such, high quality broadband X-ray spectra are critical to studying the reflected emission. Indeed, with coordinated *XMM–Newton* + *NuSTAR* coverage it is possible to identify the reflected emission from the disc even in cases with complex (and variable) absorption (*e.g.* Risaliti et al. 2013; Walton et al. 2014, 2018; Madathil-Pottayil et al. 2025, submitted).

Nevertheless, sources with low obscuration undeniably provide the best view of the disc reflection features, and are thus particularly valuable for studies of the inner geometry of AGN and SMBH spin measurements. In addition to the broad iron emission and the Compton hump, unobscured radio-quiet AGN with appreciable accretion rates are ubiquitously seen to exhibit a relatively smooth excess of emission over the extrapolation of the hard X-ray continuum (determined above 2 keV) down to lower energies (*e.g.* Arnaud et al. 1985; Gierliński & Done 2004; Miniutti et al. 2009). This is commonly referred to as the 'soft excess'. The nature of this emission has been hotly debated since its discovery, but one of the two leading models discussed in the recent literature interprets the soft excess as another part of the reflection spectrum from the inner disc (Crummy et al. 2006; Walton et al. 2013; García et al. 2019). Originally this model focused mainly on the forest of emission lines also present in the reflection spectrum at energies $\lesssim$2 keV for a broad range of ionization states, which can blend together into a relatively smooth emission feature owing to the relativistic broadening of all of these lines. More recently, though, reflection models which include the density of the reflector as a free parameter have become available. This has proven to be a key development, as allowing for disc densities in the $n \gtrsim 10^{16}$ cm^{-3} regime[1] – as predicted by disc–corona models for a broad range of mass/accretion rate parameter space (Svensson & Zdziarski 1994) – shifts the low-energy free–free emission in the reflection spectrum up into the observed bandpass, contributing further soft X-ray flux in addition to the emission lines (García et al. 2016). The reflection interpretation has subsequently evolved to include both aspects in its treatment of the soft excess (*e.g.* Jiang et al. 2019a; Mallick et al. 2022).

The other leading model invokes a second, cooler, optically-thick corona to explain the soft excess (Done et al. 2012; Rózańska et al. 2015; Petrucci et al. 2020). This is typically interpreted within the framework of a radially-stratified accretion flow. In these models a slab of optically thick 'warm' Comptonizing material shrouds the inner regions of the blackbody emitting disc, producing the soft excess, in addition to the (even more centrally located) 'hot' corona that produces the hard X-ray emission and the 'standard' disc that emerges at larger radii. As such, this model treats the soft excess as an additional, distinct emission component contributing to the X-ray spectrum.

As a potential part of the disc reflection spectrum, understanding the origin of the soft excess has a significant impact on our ability to measure SMBH spin (and place other geometric constraints on AGN accretion flows). Temporal lags consistent with the soft excess responding to changes in the higher energy continuum emission have been seen in many cases (Fabian et al. 2009; Cackett et al. 2013; De Marco et al. 2013; Alston et al. 2020), and have a natural explanation as reverberation within the reflection interpretation. An origin that is at least partially atomic also naturally explains the apparent consistency of the 'temperature' seen for the soft excess over many orders of magnitude in both black hole mass and accretion rate when treated as a thermal component (*e.g.* Gierliński & Done 2004; Miniutti et al. 2009; Bianchi et al. 2009). However, with the availability of high S/N broad-band spectra in the *NuSTAR* era there have been conflicting claims in the literature over whether the reflection interpretation can reproduce the broad-band data, with some analyses suggesting that it can (*e.g.* Jiang et al. 2018; Xu et al. 2021; Madathil-Pottayil et al. 2024), and others suggesting that it cannot (even in the era of variable density reflection models; *e.g.* Porquet et al. 2018, 2024; Ursini et al. 2020b). In contrast, the 'warm' Comptonization model rarely has trouble reproducing the spectral data (*e.g.* Mehdipour et al. 2015; Petrucci et al. 2018; Middei et al. 2020), as the soft and hard spectral components are disconnected. As such, the nature of the soft excess remains unclear, and it may even be possible that both relativistic reflection and warm Comptonisation are at play (Xiang et al. 2022).

In order to explore these issues further, we obtained the first broadband X-ray observation of PG 1426+015 – taken with *XMM–Newton* (Jansen et al. 2001) and *NuSTAR* (Harrison et al. 2013) in coordination – and present a detailed analysis of these broadband data in this work. PG 1426+015 is a nearby ($z = 0.08657$), radio-quiet Seyfert-1 AGN which currently stands out among Seyfert galaxies as having the largest reverberation-mapped mass of any source included in the AGN Black Hole Mass Database (Bentz & Katz 2015), with $\log[m_{\rm BH}] = 9.01^{+0.11}_{-0.16}$ (Kaspi et al. 2000; Peterson et al. 2004), where $m_{\rm BH}$ is the black hole mass in solar units (*i.e.* $m_{\rm BH} = M_{\rm BH}/M_{\odot}$). The source has a bolometric luminosity of $L_{\rm bol} \sim 5 \times 10^{45}$ erg s^{-1} (Peterson et al. 2004),[2] corresponding to an Eddington ratio of $L_{\rm bol}/L_{\rm E} \sim 0.04$. Although it has received relatively little attention in the X-ray regime to date, PG 1426+015 appears to be a rare example of a 'bare' Seyfert, with no obvious X-ray absorption beyond the Galactic column. Similar to other bare Seyferts, PG 1426+015 shows clear evidence for a soft excess below ∼2 keV (Porquet et al. 2004; Page et al. 2004). In terms of the ongoing efforts to populate the mass versus spin plane for AGN, PG 1426+015 is therefore a source of particular interest, as there are very few high-mass AGN with robust spin constraints; currently the only robust spin constraints for AGN likely to be powered by black holes of mass 10^9 M$_{\odot}$ or above come from H1821+643 (Sisk-Reynés et al. 2022) and Q2237+305 (Reynolds et al. 2014). Furthermore, the unobscured nature of PG 1426+015 provides an ideal opportunity to search for the key reflection features needed to make such measurements and further explore whether the reflection interpretation can successfully reproduce the soft excess.

The rest of the paper is structured as follows: Section 2 details our data reduction and Section 3 then presents our spectral analysis of the data, touching on the low energy grating data, the iron Kα band and the broad-band continuum in turn. We then discuss our results in Section 4 and summarize our conclusions in Section 5.

[1]Most reflection models had previously adopted a fixed density of $n = 10^{15}$ cm^{-3} (*e.g.* Ross & Fabian 2005; García & Kallman 2010).

[2]Based on a 5100Å luminosity of $\log[L_{5100}/(\text{erg s}^{-1})] = 44.72$, and the 5100 Å bolometric correction of 9 adopted in that work.

Table 1. Details of the coordinated *XMM–Newton* and *NuSTAR* observation of PG 1426+015 considered in this work.

Mission	OBSID	Start Date	Good Exposure[a]
NuSTAR	60501049002	2020-01-23	105
XMM-Newton	0852210101	2020-01-24	71/99/101

Notes. [a]Exposures are given in ks, and for *XMM–Newton* are listed for the EPIC-pn/MOS/RGS detectors after background flaring has been excised. Note that all EPIC detectors are operated in SW mode, resulting in the smaller good exposure for EPIC-pn (which has a ∼70% livetime in this mode).

2 OBSERVATIONS AND DATA REDUCTION

NuSTAR and *XMM–Newton* performed a coordinated observation of PG 1426+015 in 2020 January; a summary of these observations is given in Table 1.

2.1 *XMM–Newton*

The *XMM–Newton* data were reduced using SAS v18.0.0. We cleaned the raw observation files for the EPIC detectors as standard, using EPCHAIN for the EPIC-pn detector (Strüder et al. 2001) and EMCHAIN for the EPIC–MOS detectors (Turner et al. 2001). All of the EPIC detectors were operated in Small Window (SW) mode in order to minimize the risk of pile-up. Source and background products (*i.e.* spectra and light curves) were extracted from the resulting cleaned eventfiles with XMMSELECT. We use a circular region of radius 35–40 arcsec for the source aperture (the former for EPIC-pn, the latter for EPIC–MOS), and a larger region of blank sky to estimate the background. For the EPIC-pn detector the background region is placed on the same chip as PG 1426+015, but the use of small window mode means this is not possible for the EPIC–MOS detectors, and so these regions are placed on adjacent chips. As recommended, periods of particularly high background were excluded from our analysis; for these data, this just removes a few ks of exposure right at the end of the observation. We only include single and double patterned events for EPIC-pn (PATTERN ≤ 4) and single to quadruple patterned events for EPIC–MOS (PATTERN ≤ 12) in our analysis, and the appropriate instrumental response files were generated for each detector using RMFGEN for the redistribution matrices and ARFGEN for the ancillary response files. Although we performed the reduction for each of the two EPIC–MOS units, the spectral data from these detectors were then combined into a single EPIC–MOS spectrum using ADDASCASPEC. Source light curves were corrected for PSF losses based on the size of the source aperture using EPICLCCORR. The total count rates (∼5–6.5 ct s^{-1} for EPIC-pn and ∼1.2–1.7 ct s^{-1} for each EPIC–MOS detector) were sufficiently low that pile up is of no concern owing to the use of SW mode.

The data from the Reflection Grating Spectrometer (RGS; den Herder et al. 2001) were reduced using RGSPROC, which both cleans the raw event files and extracts the spectral products and their associated instrumental response files. Both of the RGS units were operated in standard Spectroscopy mode, and we used both the standard source and background regions. As with the EPIC data, periods of particularly high background were excluded. The net source count rates were ∼0.15 ct s^{-1} for each RGS detector, and the data from RGS1 and RGS2 were merged into a single RGS spectrum using the RGSCOMBINE routine (after confirming there were no notable differences between them over their common energy coverage).

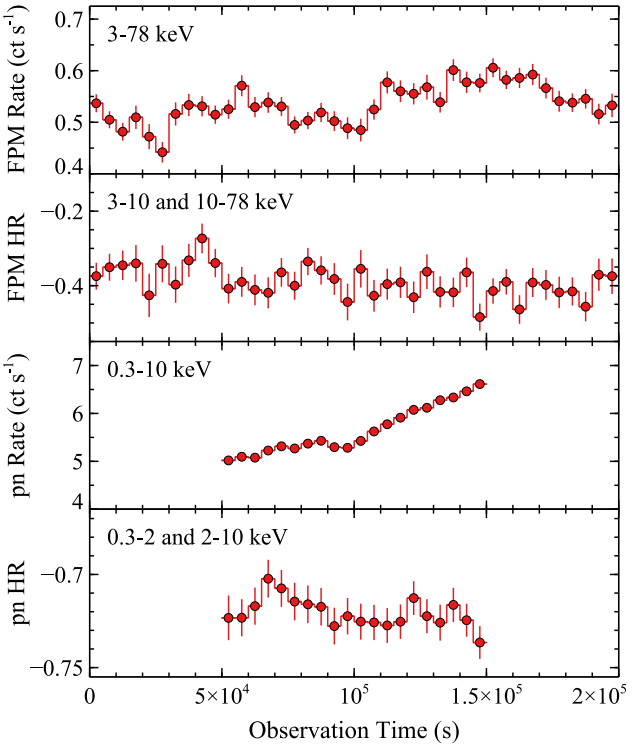

Figure 1. Lightcurves and hardness ratios (HRs) for the *NuSTAR* (top two panels) and *XMM–Newton* (bottom two panels) observations considered here. The HRs shown here are defined as $(H - S)/(H + S)$, where H and S are the count rates in the harder and softer of the indicated bands, respectively, and the bands used are defined in the observed frame. For *NuSTAR* we show the combined data for FPMA+FPMB, and for *XMM–Newton* we show the data for the EPIC-pn detector.

2.2 *NuSTAR*

The *NuSTAR* data were reduced following standard procedures with the *NuSTAR* data analysis software (NUSTARDAS) v1.9.2, and *NuSTAR* calibration data base v20200726. The unfiltered event files for both focal plane modules (FPMs) A and B were cleaned with NUPIPELINE, using the standard depth correction to reduce the internal high-energy background. Passages through the South Atlantic Anomaly were excluded using the minimal, default settings. Source products and their associated instrumental response files were then extracted for each module using circular regions of radius 80″ with NUPRODUCTS. As with the *XMM–Newton* data the background was estimated from larger regions of blank sky, which were placed on the same chip as PG 1426+015. We extract both the standard 'science' data (mode 1) and the 'spacecraft science' data (mode 6; see Walton et al. 2016) in order to maximise the signal-to-noise (S/N); the mode 6 data provide ∼10 per cent of the total *NuSTAR* exposure quoted in Table 1 in this case. While the optics temperatures indicate this observation could potentially be affected by the tear in the thermal blanket that was recently identified (Madsen et al. 2020), which can degrade the consistency of the two FPMs at the lowest energies covered by *NuSTAR*, we see no evidence for disagreement between FPMA and FPMB in this case and so we use the *NuSTAR* data over the full 3–78 keV bandpass. Finally, we merged the FPMA and FPMB data into a combined FPM spectrum using ADDASCASPEC, and similarly summed the FPMA and FPMB lightcurves into a combined FPM light curve using LCURVE.

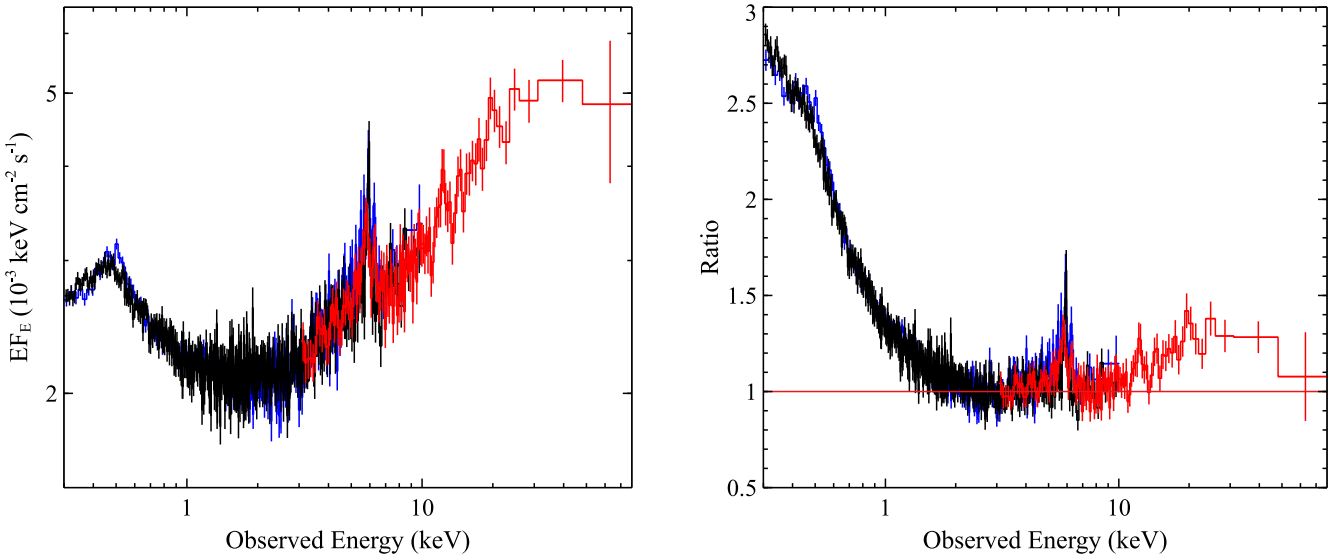

Figure 2. Left panel: the broadband *XMM–Newton* +*N uSTAR* spectrum of PG 1426+015 (after being unfolded through a model that is constant in EF_E). The *XMM–Newton* data are shown in black and blue (EPIC-pn and EPIC-MOS, respectively) and the *NuSTAR* data are shown in red (combined FPMA and FPMB data). Right panel: residuals to a simple powerlaw continuum ($\Gamma = 1.76$), modified by Galactic absorption and applied to the broad-band data over the 2–4, 7–10, and 50–78 keV energy ranges (bands that should be dominated by the primary AGN continuum). A strong and smooth soft excess can be seen below ∼2 keV, as is also seen in the archival *XMM–Newton* data (Porquet et al. 2004; Page et al. 2004) and other unobscured AGN (*e.g.* Walton et al. 2013). In addition, iron emission can clearly be seen, along with a hard excess above ∼10 keV indicating the presence of a reflection continuum. Note that the data in both panels have been rebinned for visual clarity.

3 X-RAY SPECTROSCOPY

Limited variability is seen by either *XMM–Newton* or *NuSTAR* during this new observation (see Fig. 1); the data show a systematic rising trend, with an overall increase in flux of ∼20–30 per cent seen in both cases, but there is no evidence for strong associated spectral variability based on lightcurves extracted in the 0.3–2.0 and 2.0–10.0 keV bands for *XMM–Newton*, and in the 3–10 and 10–78 keV bands for *NuSTAR*. We therefore focus our analysis on the time-averaged data. All of the EPIC and *NuSTAR* data sets are binned to a minimum signal-to-noise (S/N) of 5. Our spectral analysis is performed with XSPEC (Arnaud 1996), and unless stated otherwise we fit the data by minimizing the χ^2 statistic. All of our spectral models include absorption from the Galactic column in the direction of PG 1426+015 ($N_{\rm H,Gal} = 2.6 \times 10^{20}$ cm^{-2}; HI4PI Collaboration 2016). This is modelled with the TBABS absorption code (Wilms et al. 2000), and we assume the absorption cross-sections of Verner et al. (1996) and the solar abundances of Grevesse & Sauval (1998), since these abundances are implicitly assumed in many of the spectral models we use throughout this work. Additionally, for the fits that involve both the *XMM–Newton* and *NuSTAR* data (Sections 3.2–3.4), we allow for multiplicative normalization constants to vary for the EPIC–MOS and FPM data (with the constant for the EPIC-pn data fixed to unity) to account for any cross-calibration issues, as well as the slightly different durations of the exposures, fixing the EPIC-pn detector at unity. These are always found to be within ∼5 per cent of unity.

The broad-band spectrum is shown in Fig. 2 (left panel). In order to highlight the main features present in the spectrum, we also show the data relative to a simple powerlaw continuum, fit to the 2–4, 7–10, and 50–78 keV energy bands (rest frame), as has become standard since these energy ranges should be dominated by the primary AGN continuum. In general, the spectrum is moderately hard, rising in EF_E space above ∼2 keV; the best-fitting photon index in the powerlaw model is $\Gamma = 1.76$, fairly typical for AGN at moderate accretion rates (*e.g.* Brightman et al. 2013; Ricci et al. 2017). At lower energies a strong soft excess is present, as seen in the short archival *XMM–Newton* observation (Porquet et al. 2004; Page et al. 2004), and there is no indication for any additional absorption associated with PG 1426+015 in the EPIC data. Iron emission is also clearly seen at ∼6.4 keV in the rest frame of PG 1426+015, and there is a hard excess seen above 10 keV clearly demonstrating the presence of a high-energy reflection continuum (i.e. the 'Compton hump').

3.1 The RGS Data

Given the apparent lack of absorption in the EPIC data, before embarking on a detailed analysis of the broadband spectrum we first inspect the RGS data in order to robustly confirm the nature of PG 1426+015 as a 'bare' Seyfert. In order to do so, we fit the RGS data with a phenomenological continuum model consisting of a blackbody and a powerlaw, both of which are modified by Galactic absorption. PG 1426+015 is well detected in the RGS data over the 0.4–2.0 keV band in the observed frame. Owing to the lower count rates and higher resolution in comparison to the EPIC data, we bin the RGS data to a minimum of 1 count per bin to facilitate the use of the Cash statistic[3] (Cash 1979) within XSPEC while retaining the maximum spectral resolution. Our simple continuum describes the RGS data well (see Fig. 3), with $C = 2518$ for 2433 deg. of freedom (DoF). We find a blackbody temperature of $kT = 0.11 \pm 0.01$ keV, broadly similar to the temperatures seen for other AGN when the soft excess is modelled as a blackbody (*e.g.* Gierliński & Done 2004;

[3]This is functionally similar to the χ^2 statistic, but is defined specifically for use with measurement errors that are dominated by Poisson counting statistics (instead of assuming Gaussian errors), properly accounting for the asymmetric errors associated with the low-count regime relevant for the RGS data analysed here.

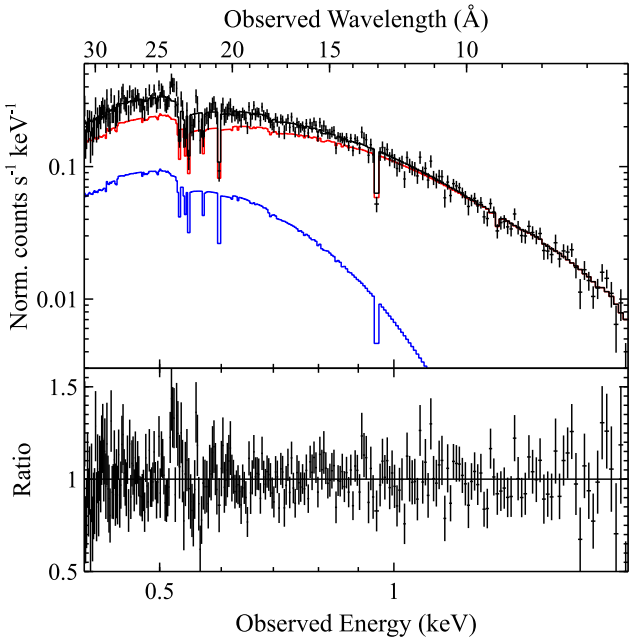

Figure 3. The fit to the RGS data with a simple phenomenological continuum model consisting of a blackbody and a power law, modified by only Galactic absorption. The top panel shows the fit to the raw data, with the black, blue and red lines showing the total model, the blackbody and the power law, respectively. The bottom panel shows the data/model ratio for this model. The data have been re-binned for visual purposes.

Crummy et al. 2006; Miniutti et al. 2009). Even with the blackbody included, we find a softer photon index of $\Gamma = 2.20 \pm 0.15$ in the RGS band than seen above 2 keV in the EPIC data.

We then search for evidence for any atomic features (either in absorption or emission) by scanning a Gaussian feature across the majority of the observed bandpass. Formally, we step the line energy across the 6.2–24.8 Å wavelength range (∼0.5–2.0 keV) in the rest-frame of PG 1426+015 in steps of 0.04 Å, broadly equivalent to the spectral resolution of the RGS data considered here. We explored a range of values for the line broadening ranging from 100–10 000 km s^{-1}, similar to *e.g.* Kosec et al. (2020), but only show a few examples in Fig. 4 for illustration. At each step we fit for the line normalization, which can be either positive (emission) or negative (absorption). The only feature of any note is an emission feature at a rest-frame energy of ∼0.57 keV, which can be identified as the O VII Ly α triplet. Modelling this as a single line with a full set of free parameters, the fit is improved by $\Delta C = 20$ for three additional free parameters, and we find a line energy, width and equivalent width of $E = 569^{+3}_{-6}$ eV, $\sigma = 5.4^{+2.4}_{-1.8}$ eV (corresponding to a line broadening of ∼3000 km s^{-1}) and $EW = 4.7 \pm 2.1$ eV. Allowing instead for a full treatment of the fact that this feature is a triplet – fixing the line energies at 561, 569, and 574 eV for the f, i, and r transitions, respectively, and assuming a common line broadening – does not improve the fit further, and results in strong degeneracies between the different line normalizations.

Critically, though, there is no obvious indication from any of the line scans performed for any absorption beyond the Galactic column in the RGS data. We also performed some simple tests using full absorption models, rather than individual line scans. First, we allowed for the presence of a second neutral absorber at the redshift of PG 1426+015, assuming solar abundances. This offered no improvement to the fit, and we found an upper limit on the column density of $N_{\rm H} < 8 \times 10^{19}$ cm^{-2}. We also allowed for an ionized absorber using XSTAR (Kallman & Bautista 2001), relying on a pre-calculated grid of absorption models from Walton et al. (2020) computed assuming a power law ionizing continuum with $\Gamma = 2$ and a velocity broadening of 100 km s^{-1} (fairly typical of 'warm' absorbers seen in other AGN; *e.g.* Laha et al. 2014). The absorber is allowed to be blueshifted relative to PG 1426+015, and we again assume solar abundances[4]. This also only offered marginal improvements in the fit, and across a range of ionization parameters spanning $\log[\xi/({\rm erg\ cm\ s^{-1}})] = 0.0$–3.0 (also typical for warm absorbers), we always find upper limits on the column density of $N_{\rm H} \lesssim 7 \times 10^{21}$ cm^{-2}; the upper limits as a function of ξ are shown in Fig. 5 (note that the XSTAR grid itself has a lower bound on the column density of 10^{20} cm^{-2}). Here, ξ has its usual definition: $\xi = L_{\rm ion}/nR^2$, where $L_{\rm ion}$ is the ionizing luminosity, n is the density of the absorber and R is the distance to the ionizing source. Taken altogether, we conclude that these tests confirm PG 1426+015 as a rare example of an essentially completely bare AGN. As such, we do not consider the RGS data any further here.

3.2 The Iron *K* band

We also present an inspection of the iron K band to test for the presence of relativistic reflection. In Fig. 6, we show a zoom-in on the 2–10 keV for the power-law fit to the high-energy data described above (*i.e.* $\Gamma = 1.76$). The combined data indicate the presence of a broad, relativistic component to the iron line, in addition to a narrow core.

In order to assess the presence of this broad component we test two models for the 2–10 keV band, fit to the combined *XMM–Newton* + *NuSTAR* data simultaneously: first, a power-law continuum with a narrow Gaussian emission line at 6.4 keV (in the rest-frame of PG 1426+015), and second the same model with a relativistic line added. In the latter case, we use the RELLINE model (Dauser et al. 2010). For the RELLINE component, we allow the line energy, the black hole spin and the disc inclination to vary (although the line energy is restricted to 6.4–6.97 keV, corresponding to neutral and hydrogen-like iron), and we assume a power-law emissivity profile, with $\epsilon(r) \propto r^{-q}$, where the emissivity index q is also a free parameter. Although the simpler model (power law with a narrow Gaussian) fits the data fairly well, with $\chi^2 = 1527$ for 1377 deg of freedom (DoF), the inclusion of the RELLINE component further improves the fit by $\Delta\chi^2 = 69$ for 5 extra free parameters. This suggests a very significant statistical improvement. The narrow core is consistent with neutral iron, with an energy of $E = 6.415 \pm 0.015$ keV, and has an equivalent width of $EW = 66 \pm 16$ eV, typical of other unobscured, radio-quiet AGN (*e.g.* Bianchi et al. 2007). The broad, relativistic component has $EW = 200 \pm 60$ eV, similar to that expected for standard illumination of an accretion disc (*e.g.* George & Fabian 1991).

In order to assess the statistical significance of the broad iron component we performed a series of Monte Carlo simulations, largely following a similar approach to Walton et al. (2015). In short, using the fakeit command in XSPEC, we simulated 10 000 sets of *XMM–Newton* and *NuSTAR* spectra with the same characteristics (exposures, backgrounds, binning criterion) as the real data, using the best-fitting model without the RELLINE component (*i.e.* just a power-law continuum with Galactic absorption and a narrow iron emission line) as our input. We then model these data sets over

[4]XSTAR uses the solar abundance set of Grevesse & Sauval (1998).

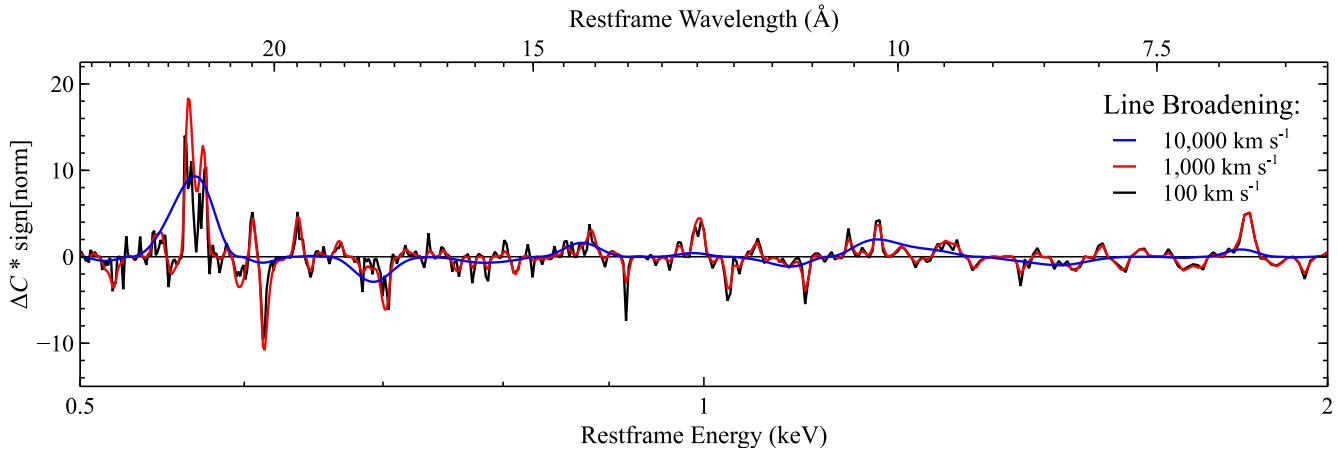

Figure 4. The results from a set of Gaussian line scans applied to the RGS data, taking the continuum fit shown in Fig. 3 as our baseline model, and assuming a few different line widths for illustration. Line energies are scanned across the 6.2–24.8 Å bandpass in steps of 0.04 Å (roughly the spectral resolution of the 1st order RGS data considered here), with the improvement (ΔC) noted for each step. Positive values of ΔC indicate emission features, and negative values indicate absorption. The only feature of any note is O VII emission at 0.57 keV.

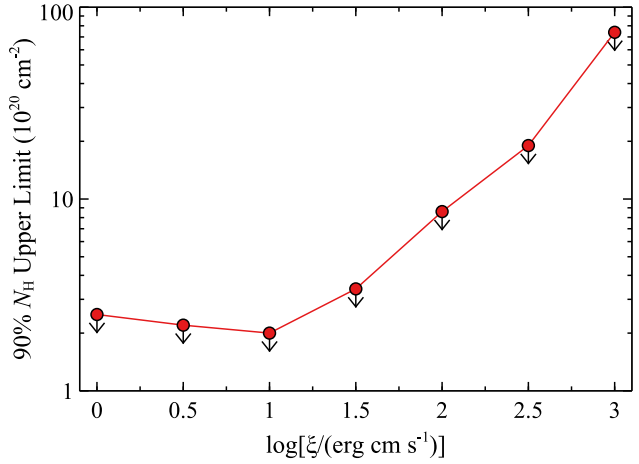

Figure 5. Upper limits from the RGS data on the column density of any ionized absorption towards PG 1426+015 as a function of ionisation parameter. These have been calculated using an XSTAR absorption model that assumes a $\Gamma = 2$ power law ionizing continuum, a velocity broadening of 100 km s^{-1} and solar abundances.

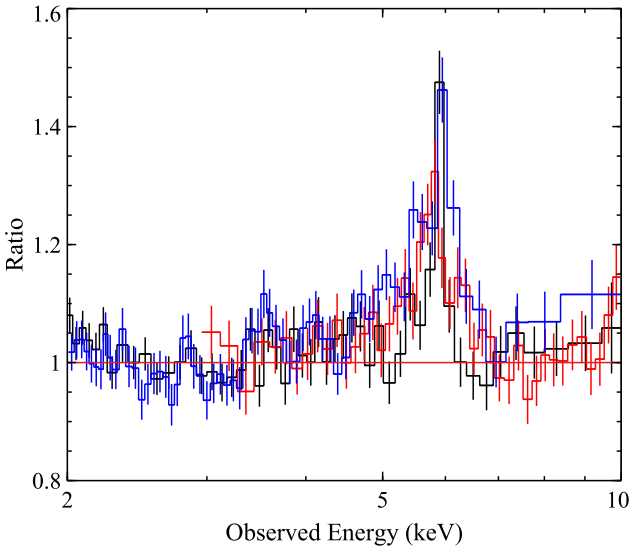

Figure 6. A zoom-in on the 2–10 keV band for the data/model ratio to the simple power-law continuum also shown in Fig. 2, highlighting the iron K residuals. The colours have the same meaning as Fig. 2, and the data have again been rebinned for visual clarity. Overall, the data appear to show evidence for both a narrow core to the iron emission, and a broad, relativistic component underlying this. However, regarding the latter, there is some disagreement between the different detectors; notably the broad component is not as obvious in the EPIC-pn data. Nevertheless, statistical analysis indicates this broad component is significantly detected when considering all of the available data (see Section 3.2).

the 2–10 keV band before and after including an additional RELLINE component, determining the improvement in χ^2 in order to assess the probability of obtaining the observed $\Delta\chi^2$ by chance. In these analyses, the RELLINE component is treated in exactly the same way as in our analysis of the real data. Of the 10 000 data sets simulated, none show a chance improvement equivalent to or greater than that observed. In fact, the maximum improvement we obtain by chance in these simulations is $\Delta\chi^2 = 24.3$, significantly below that seen in the real data. This implies the formal detection significance of the broad iron component comfortably exceeds the 4σ level, strongly supporting the visual impression that a relativistic component to the iron line is present in PG 1426+015.

3.3 Hard X-ray modelling

Having established the presence of relativistic disc reflection in the spectrum of PG 1426+015 (in addition to the relativistic iron line discussed in the previous section, we also note again the presence of a clear Compton hump in the broad-band residuals shown in Fig. 2), we now bring in the higher energy *NuSTAR* data and model the hard X-ray data (>2 keV in the rest-frame of PG 1426+015) with physical reflection models. In order to describe the relativistic disc reflection we make use of the two primary reflection models used in the literature: the XILLVER model (García & Kallman 2010) and the REFLIONX model (Ross & Fabian 2005). In both cases, the relativistic effects relevant to the innermost accretion disc are

applied by convolving these reflection models with the RELCONV model (Dauser et al. 2010).

The self-consistent combination of RELCONV and XILLVER is implemented within the RELXILL family of models (García et al. 2014; we make use of v2.3 here. Specifically, we use the RELXILLLP_CP model, which adopts the NTHCOMP thermal Comptonization model (Zdziarski et al. 1996; Zycki et al. 1999) as the ionizing continuum, and assumes a lamppost geometry for the disc–corona system. This geometry is somewhat simplistic, but its use nevertheless has some advantages in that it allows us to exclude regions of parameter space that would typically be considered non-physical (*e.g.* a very steep radial emissivity profile and a non-rotating black hole) and it also allows for a physical interpretation of the reflection fraction, $R_{\rm frac}$, which determines the relative normalizations of the ionizing continuum and the reflected emission (see Dauser et al. 2016). We note explicitly that the RELXILLLP_CP model includes both the contributions from the ionizing continuum and the reflection from the accretion disc. The NTHCOMP continuum is characterized by the photon index and the electron temperature of the Comptonizing region. The other key parameters associated with the reflection (in addition to $R_{\rm frac}$) included in the model are the spin of the black hole (a^*), the inclination, density, inner and outer radii, iron abundance[5] and ionization state of the disc (i, n, $R_{\rm in}$, $R_{\rm out}$, $A_{\rm Fe}$, ξ), and the height of the X-ray source above the spin axis (h). In this analysis, we assume that the accretion disc extends down to the innermost stable circular orbit (ISCO), and set the outer radius of the disc to the maximum value allowed by the model (1000 $R_{\rm G}$, where $R_{\rm G} = GM/c^2$ is the gravitational radius). We also allow for the treatment of returning radiation included in the latest versions of the model (see Dauser et al. 2022), and for simplicity in these hard X-ray fits we also assume a 'standard' disc density of $n = 10^{15}$ cm^{-3}.

The model utilizing REFLIONX for the disc reflection has most of the same parameters as described above. We again make use of a version of REFLIONX that assumes an NTHCOMP ionizing continuum, although here the primary continuum needs to be treated separately and so a further NTHCOMP component is included in the model. The parameters for the primary continuum are linked to those of the REFLIONX model; in the case of the electron temperature, we do so after accounting for the gravitational redshift implied by the combination of a^* and h, since with the model setup utilized here the temperature parameter for the REFLIONX component is evaluated in the rest frame of the corona while the temperature parameter for the NTHCOMP component is evaluated in the frame of an external observer. We also retain the main assumptions outlined above, and again assume a lamppost geometry for the corona (through the use of the RELCONV_LP convolution model specifically), although since the reflection and relativistic blurring components are distinct model components here there is no treatment of returning radiation considered.

As the X-ray spectrum of PG 1426+015 also shows a clear narrow core to the iron emission (Fig. 6), we also allow for the presence of more distant reprocessing (in addtion to the disc reflection) by more distant material. Here, we use the BORUS model (Baloković et al. 2018), a physically self-consistent model for reprocessing in a distant torus-like structure (formally the geometry is spherical with conical polar cutouts). The version we use also adopts an NTHCOMP model for the ionizing continuum, and we link these parameters to those of the disc reflection components in the two models we consider here (again, in the case of the electron temperature, we do so after accounting for the gravitational redshift implied by a^* and h). The other key parameters are the column density through the torus ($N_{\rm H}$; note that BORUS allows for both the Compton-thin and Compton-thick regimes), its covering factor ($C_{\rm tor} = \Omega_{\rm tor}/4\pi$, where $\Omega_{\rm tor}$ is the solid angle subtended by the torus, such that a spherical obscurer would have $C_{\rm tor} = 1$) and iron abundance ($A_{\rm Fe}$), and the angle it is viewed at (which is also linked to the inclination in the disc reflection models). Given the unobscured nature of PG 1426+015, we set a requirement that we cannot be viewing the source through the torus (i.e. $C_{\rm tor} < \cos i$). The iron abundance is also linked to the disc reflection model, after correcting for the different solar abundances assumed in these models[6].

Use of a physical torus model for the distant reflector allows the overall spectral model to incorporate the subtle changes in the strength and shape of its Compton hump as $C_{\rm tor}$ varies, and in turn help constrain this parameter. To further help constrain $C_{\rm tor}$ the BORUS normalization should in principle be linked to that of the ionizing continuum (as otherwise these two parameters are often highly degenerate, since they both control the absolute flux of the distant reflection). For the REFLIONX-based model we therefore link the BORUS normalization to that of the NTHCOMP component (after accounting for the fact that the NTHCOMP and BORUS normalizations are defined in the observed and cosmological frames, respectively, by treating the cosmological redshift on of the primary continuum with a ZASHIFT component; see Walton et al. 2022). For the RELXILLLP_CP model, though, the situation is more complicated as RELXILLLP_CP has a different definition for its normalization than NTHCOMP. Here, we therefore take the following approach: we perform an initial fit in which both $C_{\rm tor}$ and the BORUS normalization are free to vary, then determine the NTHCOMP normalization that would give the same primary continuum as implied by the RELXILLLP_CP component (after again accounting for the cosmological redshift with ZASHIFT). We then calculate a range of allowed normalizations based on this value and the fractional uncertainty on the RELXILLLP_CP normalization (as seen by an external observer) from the initial fit, and then repeat the fit with the BORUS normalization restricted to this range as our final version of the RELXILLLP_CP model.

Both models provide excellent fits to the hard X-ray data of PG 1426+015, with χ^2/Dof = 1722/1645 and 1715/1645 for the RELXILLLP_CP and the REFLIONX-based models, respectively; the best-fitting parameters are given in Table 2. We note that if we set the disc reflection fraction to zero the fit degrades by $\Delta\chi^2 = 64$ and 71 for 4 fewer free parameters, further supporting the presence of relativistic reflection. Both models show consistent solutions (although the REFLIONX model allows for a broader acceptable parameter space), and so we only show the relative contributions of the different model components (and the quality of the fit via the data/model ratio) for the RELXILLLP_CP model in Fig. 7). Even though the disc reflection is well detected, only very loose constraints can be placed on the spin parameter using only the hard X-ray data, with essentially the full range of prograde values permitted at the 90 per cent level by both models. The inclination constraints provided by both models are sensible for an unobscured AGN in the context of the unified model (*e.g.* Antonucci 1993). The best-fitting

[5]The rest of the elements are assumed to have solar abundances.

[6]The RELXILL family of models also adopts the solar abundances of Grevesse & Sauval (1998), the REFLIONX model adopts the solar abundances of Morrison & McCammon (1983), and the BORUS model adopts the solar abundances of Anders & Grevesse (1989). The iron abundance (relative to hydrogen) is a factor of 0.68 and 0.71 lower in the first two abundance sets, respectively, than in the latter, so these are the correction factors we apply.

Table 2. Parameter constraints for the disc reflection model fit to the hard X-ray data available for PG 1426+015.

Model component	Parameter		RELXILLLP_CP	RELCONV_LP⊗REFLIONX
Primary continuum	Γ		$1.92^{+0.04}_{-0.05}$	$1.91^{+0.04}_{-0.16}$
(NTHCOMP)	kT_e[a]	(keV)	> 120	> 60
	Norm[b]	(10^{-3})	–	$2.1^{+0.1}_{-1.1}$
Disc reflection	a^*		> -0.17	> 0.07
(RELXILLLP_CP or	i	(°)	33 ± 3	< 39
RELCONV_LP⊗REFLIONX)	h	$9R_G$)	< 7.3	< 4.8
	A_{Fe}	(solar)	$1.7^{+0.6}_{-0.5}$	$1.7^{+0.3}_{-0.9}$
	$\log \xi$	log(erg cm s^{-1})	$1.8^{+0.3}_{-0.2}$	$1.7^{+1.5}_{-0.3}$
	R_{frac}[c]		1.3 ± 0.4	$0.8^{+0.6}_{-0.2}$
	Norm		$1.2^{+2.8}_{-0.6} \times 10^{-4}$	$1.4^{+0.4}_{-1.1}$
Distant Reflection	$\log N_H$	log (cm^{-2})	$23.2^{+0.7}_{-0.3}$	$23.1^{+1.4}_{-0.1}$
(BORUS)	C_{tor}	(4π)	$0.82^{+0.04}_{-0.55}$	$0.32^{+0.58}_{-0.07}$
χ^2/DoF			1722/1645	1714/1645

Notes. [a] kT_e is quoted in the rest-frame of the X-ray source (*i.e.* prior to any gravitational redshift), based on the best-fitting lamppost geometry.
[b] The primary NTHCOMP continuum is incorporated within the RELXILLLP_CP model, and so does not have a separate normalization.
[c] R_{frac} is not formally a free parameter for the RELCONV_LP⊗REFLIONX model, but is calculated following the method outlined in Walton et al. (2013), i.e. via a comparison with the PEXRAV model (Magdziarz & Zdziarski 1995).

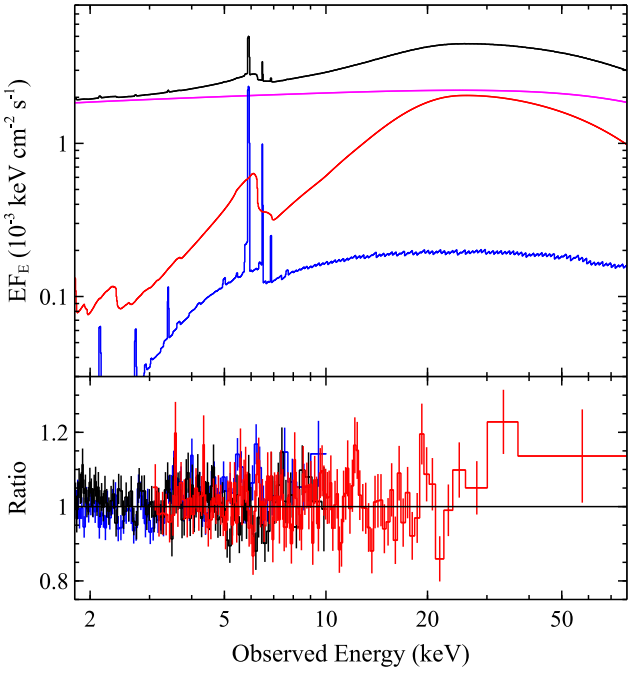

Figure 7. Top panel: the best-fitting RELXILLLP_CP + BORUS model for the hard X-ray data of PG 1426+015 (>2 keV in its rest frame). The black curve shows the total model, while the magenta, red, and blue curves show the relative contributions of the primary continuum, the relativistic disc reflection and the distant reprocessing, respectively. bottom panel: the data/model ratios for this fit. Here, the colours have the same meaning as Fig. 2, and the data have been further rebinned for visual clarity.

reflection fractions also allow reasonably standard values for a thin disc model, which should give $R_{frac} \sim 1.0$–1.7 as long as there is no strong modification of the illumination of the disc by gravitational lightbending, and also roughly solar values for the iron abundance. Despite our efforts to determine C_{tor} for the distant reflector, these values remain only poorly constrained.

3.4 Broadband modelling

Finally, given the bare nature of PG 1426+015, we also attempt to model the full broadband *XMM–Newton*+*NuSTAR* spectrum observed. Having established the presence of relativistic reflection in the spectrum of PG 1426+015 based on our analyses of the iron and hard X-ray bandpasses, we focus on exploring whether this emission can also explain the soft excess when the full *XMM–Newton* + *NuSTAR* bandpass is considered. We therefore start by re-fitting the reflection models constructed in Section 3.3, to the full observed 0.3–78 keV data, allowing for a few adjustments given the inclusion of the soft X-ray data. First, we also allow the density of the disc to be a free parameter in these fits, since the soft X-ray band is the portion of the X-ray spectrum that is most sensitive to the density of the disc. As discussed in García et al. (2016), the density parameter controls the level of free-free emission that enters into the observed soft X-ray bandpass (see also Jiang et al. 2019a; Mallick et al. 2022). This free–free emission appears as a broad, thermal-like contribution at low energies, and as the density of the disc increases more of this emission is shifted up into the soft X-ray band. Secondly, with the soft X-ray data included we also include the O VII emission detected in the RGS data (see Section 3.1). We again use a single Gaussian to account for this feature, and restrict the parameters of this component to line in the ranges found for the equivalent model in our RGS analysis.

The RELXILLLP_CP model does not provide a particularly good fit to the broad-band data, even if we relax any attempt to set the BORUS normalization based on the RELXILLLP_CP parameters (χ^2/DoF = 2366/2046). While this model can fit the data below ~30 keV well, at higher energies the model does not reproduce the overall shape of the observed spectrum, leaving a clear excess of emission at the highest energies probed by *NuSTAR* (see Fig. 8, left panels). It is possible that part of the issue here is that the lamppost geometry assumed for the corona is overly simplistic for these sources. We therefore also fit a version of this model that instead adopts a phenomenological broken power law for the emissivity profile – and thus is agnostic about the exact geometry of the corona – using the RELXILLCP model instead. Here, instead of being set solely by the height of the corona, the emissivity is described by two indices (q_{in} and q_{out}) separated by

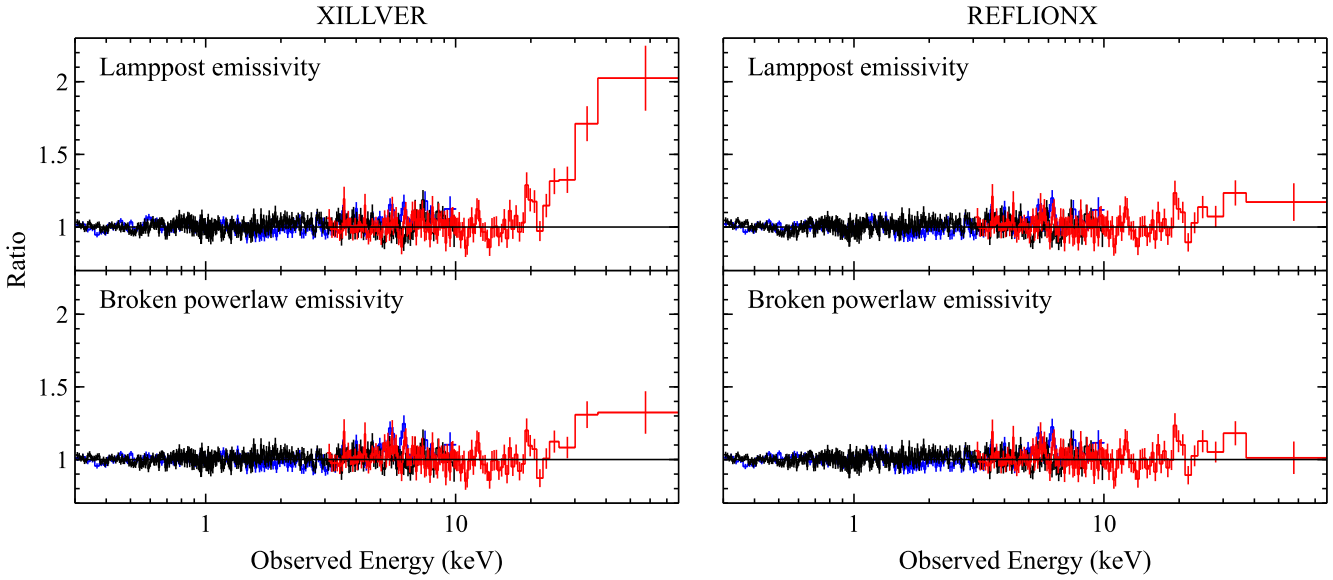

Figure 8. Data/model ratios for the set of 'basic' disc reflection models fit to the full broad-band data set. The left panels show the models based on the XILLVER reflection model (specifically using the RELXILL family of models) and the right panels show the models based on the REFLIONX models. The top panels show the fits assuming a lamppost emissivity, and the bottom panels show the fits assuming a broken power-law emissivity which is agnostic about the emission source geometry. The colours again have the same meaning as Fig. 2, and the data have been further rebinned for visual clarity.

a break radius ($R_{\rm br}$), where over a given radial regime the emissivity has the form $\epsilon(r) \propto r^{-q}$. The inner emissivity index and the break radius are free to vary in this model, while the outer index is fixed to $q_{\rm out} = 3$ (as expected for large radii; Reynolds & Begelman 1997). This model improves both the overall fit (χ^2/DoF = 2269/2045) and reduces the strength of the hard excess, but it is not able to remove it completely. Similar results have been reported for Ark 120 – another well-known bare AGN – for this model by Porquet et al. (2018), who also attempted to apply similar XILLVER-based reflection models to broadband data (also *XMM–Newton* + *NuSTAR* in coordination) and found they did not provide a satisfactory fit across the full bandpass (see also Matt et al. 2014).

In contrast, REFLIONX-based disc reflection models have no problem reproducing the broad-band data. We fit both of the variants considered for the XILLVER-based models (lamppost geometry, broken power-law emissivity), and both can simultaneously fit the soft excess, the broad iron line and the Compton hump (see Fig. 8, right panels), although the broken power-law emissivity does again provide the better statistical fit (the lamppost and broken power-law emissivities gives fits with χ^2/DoF = 2311/2047 and 2244/2046, respectively). The parameter constraints for all four of these 'basic' reflection models when applied to the broad-band data are given in Table 3[7]. We show the best-fitting REFLIONX-based model with the broken power-law emissivity profile in Fig. 9.

[7]Note that since neither of the RELXILL-based models reported here provide satisfactory fits to the broadband data with the initial fits in which both the BORUS normalisation and $C_{\rm tor}$ are free parameters, we did not undertake the subsequent step discussed for the RELXILLLP_CP fit to the hard X-ray data (Section 3.3) in which the BORUS normalisation is further limited to the range implied by the RELXILL primary continuum. Instead, we simply report the parameter constraints for these initial fits for the RELXILL-based models. In contrast, since the primary continuum and the disc reflection are separate model components in the REFLIONX-based models, the BORUS normalisation remains linked to that of the NTHCOMP components in these fits, and so is once again not a separate parameter to report.

A key difference between these XILLVER-based and REFLIONX-based models lies in the densities they return for the accretion disc, with the XILLVER-based models implying $\log(n_{\rm e}/{\rm cm}^{-3}) \sim 17$ while the REFLIONX-based models implying $\log(n_{\rm e}/{\rm cm}^{-3}) \sim 18$. As such, within the observed bandpass these XILLVER-based models include a smaller contribution from the free–free emission that increasingly dominates the soft X-ray reflection continuum at higher densities (García et al. 2016). In turn, the relative contribution from reflection in the soft band is therefore much higher for these REFLIONX-based models. Because of the weaker soft excesses in these XILLVER-based models they pivot the slope of the primary continuum to steeper values in order to successfully reproduce the soft X-ray data, as this part of the spectrum dominates the overall photon statistics of the broad-band data. This pivoting happens most severely for the lamppost variant. In turn, this drives both the reflection fraction and the iron abundance up, as the model tries as best it can to use this emission to reproduce the highest energy data seen by *NuSTAR* and softer ionising spectra tend to produce reflection spectra with weaker iron lines. In the case of the lamppost variant, this also drives the ionization parameter down (as doing so results in a harder reflection spectrum). Ultimately, though, the steeper photon indices mean that the reflected emission is still too steep to match the high energy data, resulting in the hard excesses seen in Fig. 8. Because the REFLIONX-based models are able to provide stronger soft excesses, no such pivoting of the continuum is required, and so they are able to better reproduce both the soft excess and the hard X-ray data.

The two REFLIONX-based models that do reproduce the full bandpass well occupy broadly similar areas of parameter space, and in the case of the lamppost model (where the most direct comparison can be made), the results are generally consistent with those found for the equivalent fits to the hard X-ray data (though with tighter parameter constraints now, related to the higher total S/N in the full, broad-band data set that comes from the inclusion of the *XMM–Newton* data below 2 keV). With regards to the disc reflection specifically, both imply relatively high but not extreme spins, and relatively normal reflection fractions ($R_{\rm frac} \sim 1$; Magdziarz & Zdziarski 1995; Walton

Table 3. Parameter constraints for the basic disc reflection models fit to the full broadband (*XMM–Newton* + *NuSTAR*) X-ray data available for PG 1426+015. A ∗ symbol indicates that the parameter was not free to vary in that particular model.

Model component	Parameter		RELXILLLP_CP	RELXILLCP	RELCONV_LP⊗REFLIONX	RELCONV⊗REFLIONX
Primary continuum	Γ		2.29 ± 0.01	2.00 ± 0.01	$1.82^{+0.01}_{-0.02}$	$1.82^{+0.01}_{-0.04}$
(NTHCOMP)	kT_e[a]	(keV)	> 330	> 130	69^{+25}_{-14}	90^{+130}_{-30}
	Norm[b]	(10^{-3})	–	–	$1.28^{+0.08}_{-0.04}$	1.4 ± 0.1
O VII	E	(keV)	0.569∗	0.569∗	0.569∗	0.569∗
emission[c]	σ	(eV)	5.4∗	5.4∗	5.4∗	5.4∗
	Norm	(10^{-5})	3.4∗	3.4∗	3.4∗	3.4∗
Disc reflection	a^*		$0.95^{+0.01}_{-0.02}$	> 0.99	0.89 ± 0.04	$0.77^{+0.06}_{-0.08}$
(various	i	(°)	40^{+1}_{-2}	39^{+11}_{-3}	< 37	< 24
combinations)	h	(R_G)	$2.2^{+0.3}_{-0.1}$	–	< 2.5	–
	q_{in}		–	6.4 ± 0.5	–	$4.9^{+1.1}_{-1.0}$
	R_{br}	R_G	–	$7.0^{+2.7}_{-1.2}$	–	$10.0^{+3.2}_{-1.9}$
	q_{out}		–	3.0∗	–	3.0∗
	A_{Fe}	(solar)	$3.8^{+0.3}_{-0.5}$	$1.7^{+0.2}_{-0.3}$	0.76 ± 0.04	$0.79^{+0.05}_{-0.03}$
	$\log \xi$	log (erg cm s^{-1})	< 0.1	$2.71^{+0.04}_{-0.10}$	$3.01^{+0.05}_{-0.03}$	$2.97^{+0.06}_{-0.03}$
	$\log n$	log (cm^{-3})	$17.0^{+0.1}_{-0.2}$	17.2 ± 0.1	17.98 ± 0.05	$18.0^{+0.1}_{-0.2}$
	R_{frac}[d]		7.5 ± 0.3	$3.5^{+0.5}_{-0.4}$	$1.0^{+0.5}_{-0.1}$	$1.1^{+0.1}_{-0.5}$
	Norm		$6.1^{+3.3}_{-0.9} \times 10^{-4}$	$1.9^{+0.3}_{-0.1} \times 10^{-5}$	$0.115^{+0.010}_{-0.005}$	0.11 ± 0.01
Distant reflection	$\log N_H$	log (cm^{-2})	24.7 ± 0.2	> 24.7	$23.8^{+0.2}_{-0.1}$	$23.8^{+0.2}_{-0.1}$
(BORUS)	C_{tor}		0.76 ± 0.02	$0.76^{+0.04}_{-0.13}$	$0.69^{+0.20}_{-0.11}$	$0.80^{+0.08}_{-0.10}$
	Norm	(10^{-3})	$4.0^{+0.4}_{-0.5}$	$3.4^{+0.5}_{-0.6}$	–	–
χ^2/Dof			2366/2046	2269/2045	2275/2047	2244/2046

Notes. [a]For the lamppost variants kT_e is quoted in the rest-frame of the X-ray source (*i.e.* prior to any gravitational redshift), based on the best-fitting lamppost geometry.
[b]The primary NTHCOMP continuum is incorporated within the RELXILLLP_CP model, and so does not have a separate normalization.
[c]These parameters are fixed, based on the analysis of the RGS data (see Section 3.1). The line energy is given in the rest-frame of PG 1426+015.
[d] R_{frac} is not formally a free parameter for the REFLIONX-based models, but is again calculated following the method outlined in Walton et al. (2013), i.e. via a comparison with the PEXRAV model (Magdziarz & Zdziarski 1995).

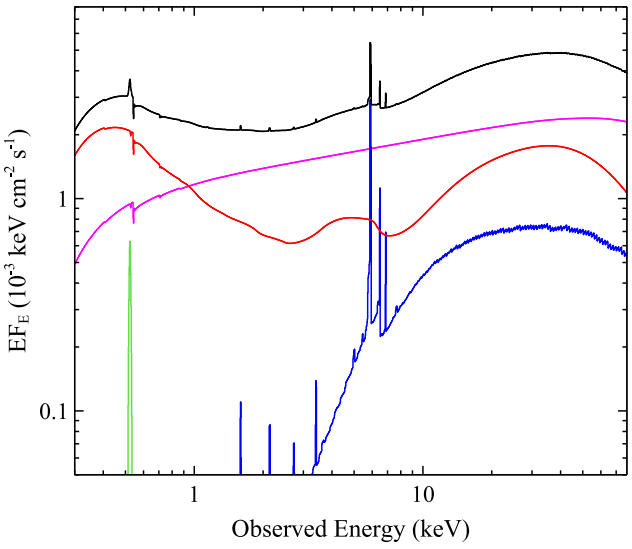

Figure 9. The best-fittig REFLIONX-based disc reflection model with a broken power-law emissivity profile, applied to the full *XMM–Newton* + *NuSTAR* broad-band data set. The colours are the same as Fig. 7 (top panel), with the narrow O VII emission additionally shown in green.

et al. 2013). The best-fitting inclinations ($i \lesssim 25°$) suggest that we are viewing the disc almost face-on; again, this is consistent with the general expectation for an AGN with such low obscuration based on the unified model (Antonucci 1993). Finally, both models also imply very similar densities for the accretion disc of $n \sim 10^{18}$ cm^{-3}, in excess of the value traditionally adopted in most older generations of reflection model (which generally assumed 10^{15} cm^{-3}; e.g. Ross & Fabian 2005; García & Kallman 2010).

3.4.1 XILLVER: the importance of oxygen

In principle, it should still be possible for XILLVER to provide a low-energy reflection continuum with a similar strength as REFLIONX by moving to higher densities than the fits in Table 3 imply. However, a key reason that the RELXILLCP model (which comes closest of the XILLVER-based models considered here to fitting the broad-band data) does not do this is that at these higher densities than reported in Table 3 XILLVER predicts the presence of an extremely strong O VIII emission line in the rest-frame reflection spectrum at the ionization parameters preferred by this model (and also the REFLIONX-based fits; $\xi \sim 1000$ erg cm s^{-1}). This results in a structure to the soft excess (even after the application of the relativistic blurring) that the data do not want. The corresponding O VIII emission in the REFLIONX model is much weaker (see Fig. 10), which also helps this model fit the broad-band data successfully. When compared against a local power-

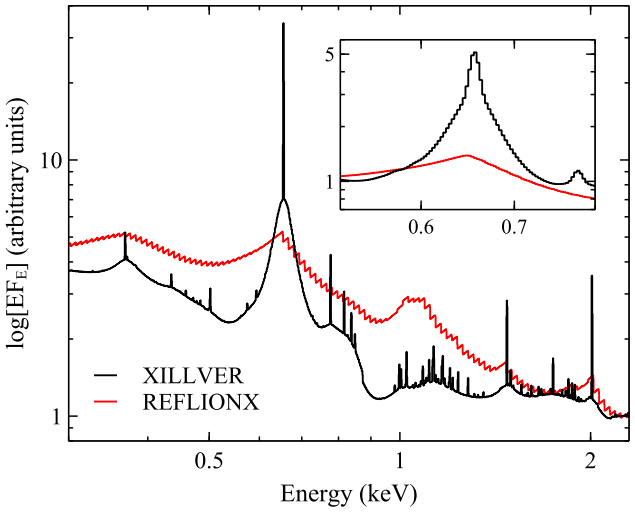

Figure 10. Main panel: A comparison of the rest-frame XILLVER (black) and REFLIONX (red) reflection models in the soft band for a density of $n = 10^{18}$ cm^{-3} and an ionization parameter of $\xi = 10^3$ erg cm s^{-1} (*i.e.* no relativistic blurring has been applied). We also assumed an NTHCOMP ionizing continuum with $\Gamma = 1.8$ and $kT_e = 60$ keV, as well as a solar iron abundance for both models, and the models have been normalized to give the same flux at 2.25 keV. The XILLVER model appears to have stronger oxygen emission at ∼0.65 keV for this parameter combination than the REFLIONX model. Note also that the REFLIONX model has a coarser internal spectral resolution, resulting in the visible saw-toothing in the main panel. Inset: The same models smoothed with a Gaussian of width 25 eV (so that they are now plotted with broadly the same resolution) and zoomed-in on the oxygen emission in question. The models are also now normalized so that the averages of the fluxes at 0.55 and 0.75 keV are the same in both cases. The quantitative comparisons discussed in the main text confirm the stronger O VIII emission in XILLVER.

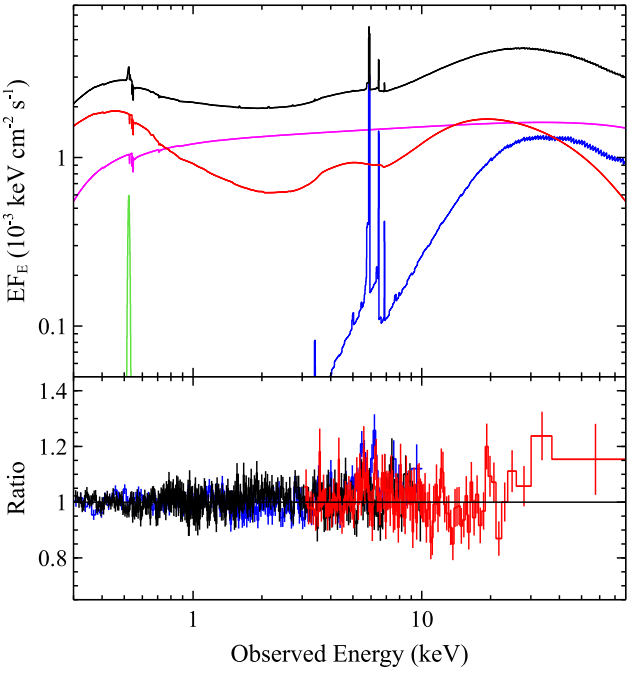

Figure 11. Top panel: the best-fit for the XILLVER-based disc reflection model where the O VIII emission in the XILLVER component is allowed to be modified by an additional GABS component to mimic a sub-solar oxygen abundance, applied to the full *XMM–Newton* + *NuSTAR* broad-band data set. The colours in both panels have the same meaning as Figs 7 and 9, and the data have again been rebinned for visual clarity.

law continuum defined between the energies 0.55 and 0.75 keV, the equivalent width of the oxygen emission in the XILLVER model is a factor of ∼3 larger than in REFLIONX. This difference in EW is in part because of the stronger soft X-ray continuum seen in REFLIONX for a given density, but also because the absolute O VIII line flux (evaluated as the flux difference between the reflection models and the local power-law continua described earlier in the 0.55–0.75 keV band) is a factor of ∼2 larger in the XILLVER_CP model for these parameters when the two models are normalized to have equal fluxes at 2.25 keV (away from the main impact of the different low-energy reflection continua in the two models and avoiding any obvious line emission)[8]. The difference in these O VIII line fluxes cannot obviously be related to the different elemental abundances the two models adopt, as their oxygen abundances (relative to Hydrogen) only differ by 10 per cent.

The above comparison between REFLIONX and XILLVER suggests that being able to adjust the strength of the oxygen emission may be an important factor in determining whether XILLVER-based models can fit broadband X-ray data from AGN successfully (and particularly the soft excess, when there is a clear view of this feature). Most reflection models allow for the iron abundance to be a free parameter, given the importance of the relativistically broadened iron line, but it is rare for reflection models to allow for non-solar oxygen abundances as well. Indeed, there is currently no version of the XILLVER model that is both suitable for use with AGN and has the oxygen abundance as a free parameter which would allow us to test this possibility directly. We therefore attempt to mimic this possibility by applying a Gaussian absorption line to the intrinsic reflection spectrum (using a GABS component) in order to remove some of the flux from the oxygen emission prior to the application of the relativistic blurring (since in this case it appears that the XILLVER model has more oxygen emission than the data wants). Doing so requires separate treatment of the reflection and the relativistic blurring, and so here we replace the RELXILLCP component with the combination NTHCOMP + RELCONV⊗[GABS×XILLVER_CP], where the XILLVER_CP component is configured to only provide reflected emission. The energy of the GABS component is fixed at 0.654 keV in the rest frame of PG 1426+015, and the width of the line is fixed at 1 eV, so the only extra free parameter is the strength of the absorption. With this model setup, we can once again directly link the BORUS normalization to that of the primary NTHCOMP continuum. Other aspects of the model setup remain the same as the equivalent model discussed in the previous section.

This model combination provides a better fit to the broadband data than the basic implementation discussed previously (χ^2/Dof = 2247/2045), and critically there is no longer a significant excess of emission at high energies. This is because the reduction in the O VIII flux means the reflection component is now more easily able to account for the soft excess by increasing the density of the disc (which is now also $n \sim 10^{18}$ cm^{-3}, similar to the REFLIONX-based fits), and subsequently the power-law continuum no longer needs to pivot to softer values to the same degree in order to fit this part of the spectrum. The best-fitting model is shown in Fig. 11, along with the data/model ratio, and the full set of parameter constraints for this model are given

[8]We also find a similar difference if we normalise the REFLIONX and XILLVER models to have the same flux over broader bandpasses of 0.1–10 keV and 0.1–1000 keV, instead of at 2.25 keV specifically.

Table 4. Parameter constraints for the XILLVER-based disc reflection model where the flux of the O VIII emission in the XILLVER component is allowed to be reduced by an additional GABS component, fit to the full broadband (*XMM–Newton* + *NuSTAR*) X-ray data. A ∗ symbol indicates that the parameter was not free to vary.

Model component	Parameter		
Primary cont.	Γ		1.92 ± 0.01
(NTHCOMP)	kT_e	(keV)	> 130
	Norm	(10^{-3})	$1.49^{+0.10}_{-0.03}$
O VII	E	(keV)	0.569∗
emission[a]	σ	(eV)	5.4∗
	Norm	(10^{-5})	3.4∗
RELCONV	a^*		0.95 ± 0.01
	i	(°)	42 ± 2
	q_{in}		$7.0^{+0.4}_{-0.5}$
	R_{br}	R_G	$6.0^{+1.0}_{-0.5}$
	q_{out}		3.0∗
GABS[b]	E	(keV)	0.654∗
	σ	(eV)	1∗
	Strength	(10^4)	> 1.5
XILLVER_CP	A_{Fe}	(solar)	$1.8^{+0.2}_{-0.1}$
	$\log \xi$	$\log(\mathrm{erg\,cm\,s^{-1}})$	$2.70^{+0.01}_{-0.05}$
	$\log n$	$\log(\mathrm{cm^{-3}})$	$18.00^{+0.02}_{-0.08}$
	R_{frac}[c]		$1.8^{+0.3}_{-0.1}$
	Norm	(10^{-5})	$4.5^{+0.6}_{-0.3}$
Distant refl.	$\log N_H$	$\log(\mathrm{cm^{-2}})$	> 24.7
(BORUS)	C_{tor}		$0.6^{+0.05}_{-0.10}$
χ^2/DoF			2247/2045

Notes [a]As before, these parameters are fixed based on the analysis of the RGS data (see Section 3.1), and the line energy is given in the rest-frame of PG 1426+015.
[b]The GABS component is applied to the XILLVER_CP component prior to the further application of RELCONV, so that the overall disc reflection component here has the form RELCONV⊗(GABS × XILLVER_CP). Again the line energy is given in the rest frame of PG 1426+015.
[c]R_{frac} is not formally a free parameter here, now that the RELCONV and XILLVER components are separated, and but is again calculated following the method outlined in Walton et al. (2013), i.e. via a comparison with the PEXRAV model (Magdziarz & Zdziarski 1995).

in Table 4. With the best-fitting parameter combination, the GABS component removes ∼half of the total O VIII flux in the XILLVER_CP component, again assessed by comparing the XILLVER_CP model against a local power-law continuum defined between 0.55 and 0.75 keV both with and without the GABS component included. This may imply that an oxygen abundance of A_O/solar ~ 0.5 would be preferred by this model, although it is also worth noting that the remaining O VIII flux would still imply that within the reflection model itself this feature has an equivalent width comparable to that of the REFLIONX model with a solar oxygen abundance. The mild remaining high-energy residuals will likely be accounted for with future variants of RELXILL/XILLVER that will incorporate the improved treatment of Compton scattering discussed in García et al. (2020), as this will result in reflection spectra with slightly higher high-energy fluxes (though we stress that this by itself would not be sufficient to account for the excesses seen in Fig. 8 without still needing to modify the strength of the oxygen emission).

We also note that a similar improvement is seen when allowing the O VIII line strength to vary for the lamppost model as well (i.e. treating the relativistic reflection as RELCONV_LP⊗[GABS × XILLVER_CP]), though as with the REFLIONX-based models the broken-power-law emissivity once again provides the superior fit (the fit for the lamppost model improves to χ^2/DoF = 2287/2046). We do not present this model in full, as the best-fitting solution is broadly similar to that already presented in Table 4, but note that the lamppost variant once again prefers a slightly higher spin parameter ($a^* > 0.99$), similar to the results seen from the REFLIONX-based models (Table 3), and the constraint on the height of the corona is broadly similar to that found for the REFLIONX-based lamppost variant ($h \lesssim 2\,R_G$).

4 DISCUSSION

PG 1426+015 is a source of notable interest, as it has the largest reverberation-mapped mass reported for any AGN to date: $\log[m_{BH}] = 9.01^{+0.11}_{-0.16}$ (Kaspi et al. 2000; Peterson et al. 2004). Furthermore, the high-resolution RGS data reported here confirm its nature as one of the relatively rare examples of a genuinely bare AGN (Section 3.1).

4.1 The soft excess

The bare nature of PG 1426+015 offers an opportunity to explore the nature of the soft excess – which is very clearly present in the spectrum of PG 1426+015 (Fig. 2) – via broad-band X-ray observations taken with *XMM–Newton* and *NuSTAR*. Together, the observations presented here provide simultaneous coverage over the 0.3–78 keV bandpass. Currently, two leading models are typically considered as the potential origins of this emission in the literature: relativistic reflection from the accretion disc, and the presence of a second, 'warm' corona (in addition to the 'hot' corona that gives rise to the primary X-ray continuum seen above 2 keV).

We have focused our work on the question of whether the relativistic reflection model can successfully fit the broad-band data set. In this model, the soft excess comes about through the combination of the low-energy emission lines predicted by ionized reflection and the appreciable free-free emission expected from dense, ionized plasma; the strong relativistic effects close to the black hole broaden and blend these features into a relatively smooth emission profile (*e.g.* Crummy et al. 2006; Walton et al. 2013; Jiang et al. 2019a; Mallick et al. 2022). We focus on this issue because, as a potential part of the reflection component from the inner accretion disc, simultaneous broadband observations such as those presented here represent the key stress test of whether this model remains plausible, and there are contrasting claims in the literature with regards to whether it can successfully fit the broadband data obtained for other bare AGN (*e.g.* Porquet et al. 2018; García et al. 2019; Ursini et al. 2020b; Xu et al. 2021; Madathil-Pottayil et al. 2024). It is worth stressing that, regardless of the nature of the soft excess, the combined *XMM–Newton* + *NuSTAR* data considered here independently confirm the presence of relativistic reflection in the spectrum of PG 1426+015: a relativistically broadened iron emission line is clearly detected (Section 3.2), and the corresponding high-energy reflected continuum is also observed (Fig. 2).

Although we have not explicitly considered the warm corona model in this work, this is simply because such fits are already presented in a separate analysis of these data, included as part of an ensemble analysis of a sample of AGN with broad-band spectra (Mallick et al. 2025). That work initially attempts to model the soft excess with relativistic reflection using XILLVER-based reflection models, finding the same issues with these fits for PG 1426+015 as discussed in Section 3.4 (and similar to prior studies of a few other sources; Porquet et al. 2018, 2024; Ursini et al. 2020b). Mallick et al.

(2025) subsequently include a warm corona to account for the soft excess in PG 1426+015, finding that this interpretation is able to successfully fit the broadband data. We therefore stress that we are not attempting to argue that this is not a viable model for the soft excess by focusing only on the reflection case.

As part of our focus on the reflection interpretation, we have chosen to test both of the leading reflection models commonly used in the recent literature: XILLVER and REFLIONX. Both of these models allow for ionized reflection, and their latest versions both also include the density of the disc as a free parameter. This is a key parameter that controls the free–free emission seen in these models at lower energies (García et al. 2016), and is therefore an important factor to consider when attempting to model the soft excess with relativistic reflection (as already highlighted by several previous authors; *e.g.* Jiang et al. 2019a; Mallick et al. 2022).

Ultimately, we find that both reflection models are able to reproduce the broadband *XMM–Newton* + *NuSTAR* data observed, including the soft excess. However, we do find an issue when initially attempting to fit the data with the XILLVER-based model, which relates to the very strong O VIII emission line predicted by this model at higher densities (much stronger than the equivalent REFLIONX model, see Section 3.4.1). The strength of this line is sufficient that it introduces structure into the model that the data do not want. Allowing a weaker O VIII emission line is required to enable the XILLVER-based model to successfully reproduce the broadband data. This same issue is likely what resulted in Porquet et al. (2018), Porquet et al. (2024) and Ursini et al. (2020a) concluding the relativistic reflection cannot reproduce both the soft excess and the hard X-ray data in other bare AGN with coordinated *XMM–Newton* + *NuSTAR* observations even when treating the disc density as a free parameter. Those analyses all used XILLVER-based reflection models, and the resulting fits leave residuals that are all qualitatively similar to those we find for the XILLVER-based models for PG 1426+015 without any modification to the oxygen emission included (Fig. 8). No such correction is required for the REFLIONX-based models, since REFLIONX typically predicts both a stronger low-energy reflection continuum and weaker O VIII emission.

In principle, there are several potential reasons that the O VIII line from the disc in PG 1426+015 could be weaker than the O VIII line predicted in the XILLVER model. An obvious astrophysical possibility is that the oxygen abundance in PG 1426+015 is below the solar value. Non-solar iron abundances have been reported for several AGN even when density of the disc is included as a free parameter (*e.g.* Mallick et al. 2018; Jiang et al. 2019a, 2022; Walton et al. 2021), so non-solar oxygen abundances may not be unreasonable. However, while this may be plausible if the XILLVER model is considered in isolation, this cannot obviously explain the differences between the XILLVER and REFLIONX models in terms of their O VIII emission, as the two models adopt similar values for the solar abundance of oxygen. The detection of the narrow O VII emission in the RGS spectrum (Section 3.1) may also argue against this possibility. A more critical issue may be that the O VIII line is a resonant line, and the radiative transfer of such emission lines is highly non-trivial, relating in particular to the re-absorption and scattering of the line photons as they emerge from the disc. The two models take different approaches to dealing with these lines, which likely explains why the two models predict different line strengths; REFLIONX treats these lines using an escape fraction approach (Ross & Fabian 2005), while XILLVER assumes these lines follow the same radiative transfer as the continuum emission, which is solved via the Feautrier method (García & Kallman 2010). As such, XILLVER does not currently account for any additional line opacity when the lines themselves have appreciable optical depths, a potential issue for the strength of the O VIII emission (though not necessarily for other key lines such as Fe K).[9] Should XILLVER end up over-predicting the O VIII emission, as is likely at least to some extent, one would need to remove some of this flux in order to produce realistic reflection spectra. Further investigation of this issue will be important to pursue in the future, but is beyond the scope of this paper.

4.2 Density of the accretion disc

Considering the different models that successfully fit the data, we find an overall constraint on the density of the disc of $\log(n_e/\mathrm{cm}^{-3}) = 18.0^{+0.1}_{-0.2}$, significantly in excess of the typical density of $\log(n_e/\mathrm{cm}^{-3}) = 15$ assumed in most prior reflection models. The only prior constraint available in the literature for PG 1426+015 comes from Jiang et al. (2019a), who find $\log[n_e/\mathrm{cm}^{-3}] < 15.9$, which is rather different to the result found here. It is worth noting, though, that this prior constraint is derived from a short snapshot observation taken with *XMM–Newton*, only providing spectral coverage up to 10 keV. These limitations meant Jiang et al. (2019a) ended up fixing several of the reflection parameters to assumed values (*e.g.* they assumed a power-law emissivity with $q = 3$), since they were otherwise unconstrained. As such the deeper, broadband data considered here likely provide more reliable constraints on the density of the disc.

In the disc–corona model of Svensson & Zdziarski (1994) the density of the inner disc is expected to be inversely proportional to the product $m_{\mathrm{BH}}\dot{m}^2(1-f)^3$, where $\dot{m}$ is the Eddington-scaled accretion rate (*i.e.* $\dot{m} = \dot{M}c^2/L_{\mathrm{E}}$) and f is the fraction of the accretion power dissipated in the corona, assuming the disc is dominated by radiation pressure. In order to place the results for PG 1426+015 in the context of this model, and the growing ensemble of reflection-based density constraints for AGN accretion discs (compiled from Jiang et al. 2019a, b, 2022; Mallick et al. 2018, 2022; García et al. 2019; Walton et al. 2021; Xu et al. 2021; Wilkins et al. 2022; Madathil-Pottayil et al. 2024), we show where PG 1426+015 lies in the $\log[n_e/\mathrm{cm}^{-3}]$ versus $\log[m_{\mathrm{BH}}\dot{m}^2]$ plane in Fig. 12 (omitting the prior density constraint presented in Jiang et al. 2019a for PG 1426+015 from the contextual data plotted to ensure this source does not appear twice). To facilitate a self-consistent comparison between our updated result for PG 1426+015 and this broader AGN sample, following Jiang et al. (2019a), we determine the value of $\log[m_{\mathrm{BH}}\dot{m}^2]$ by combining the reverberation-mapped mass constraint with the accretion rate estimated from the optical luminosity using the method outlined in Raimundo et al. (2012):

$$\frac{\dot{M}}{M_\odot\ \mathrm{yr}^{-1}} = 1.53\left(\frac{\nu L_\nu}{10^{45}\ \cos i}\right)^{3/2}\left(\frac{m_{\mathrm{BH}}}{10^8}\right)^{-1}\left(\frac{\nu}{\nu_{4392}}\right)^{-2} \quad (1)$$

Here, the monochromatic luminosity νL_ν is measured in units of erg s^{-1}, ν is the photon frequency at which this luminosity is measured and ν_{4372} is the photon frequency that corresponds to the

[9]In more detail: XILLVER uses the XSTAR routines to compute continuum and line emissivities (and opacities). By default, line emissivities are calculated assuming an optically thin medium, in which case the line emissivity scales linearly with the ion fraction and excitation rate. However, in optically thick conditions, photons are resonantly trapped and scattered, in which case the escape probability of a line scales as the inverse of the optical depth. This dependency is not currently taking into account in the XILLVER models, which can lead to an overestimation of the O VIII emission. Note, however, this effect does not affect the Fe K emission, as those are fluorescent lines involving photoionization and recombination rather bound-bound transitions.

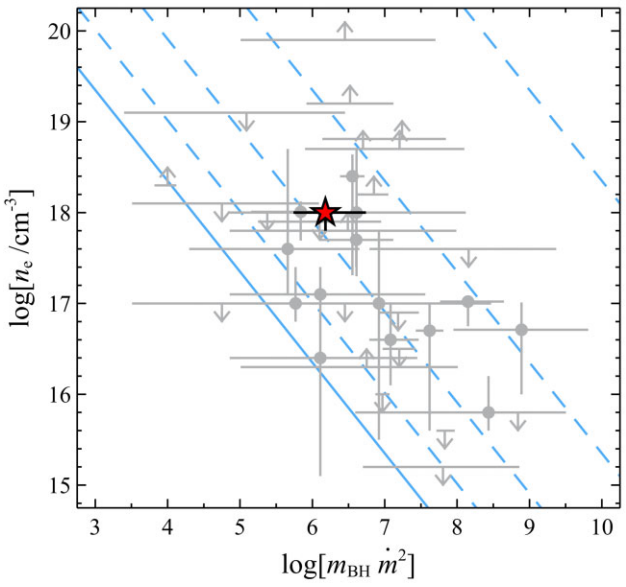

Figure 12. The position of PG 1426+015 in the $\log[n_e/\mathrm{cm}^{-3}]$ versus $\log[m_{\rm BH}\dot{m}^2]$ plane, compared to other AGN for which reflection-based density constraints for the inner disc are available. Our results for PG 1426+015 are indicated by the red star, while the broader AGN population are shown in the background as grey points (compiled from: Jiang et al. 2019a, b, 2022; Mallick et al. 2018, 2022; García et al. 2019; Walton et al. 2021; Xu et al. 2021; Wilkins et al. 2022; Madathil-Pottayil et al. 2024, 2025, submitted). Note that the prior constraint for PG 1426+015 presented in Jiang et al. (2019a) is not included as part of this comparison sample, nor are the constraints for Ark 564 or PG 1229+204 from that work (the other two sources for which UV data were used when estimating $\log[m_{\rm BH}\dot{m}^2]$; see footnote 10). The results for PG 1426+015 sit within the scatter of the loose anticorrelation between $\log[n_e/\mathrm{cm}^{-3}]$ and $\log[m_{\rm BH}\dot{m}^2]$ exhibited by these other sources. The solid blue line shows the predicted $\log[n_e/\mathrm{cm}^{-3}] \propto -\log[m_{\rm BH}\dot{m}^2]$ trend predicted by Svensson & Zdziarski (1994) for a radius just outside the inner radius of the disc (formally, we assume $R = 4R_{\rm G}$ and $R_{\rm in} = 2R_{\rm G}$, following Jiang et al. 2019a) and the limiting case where no accretion power is dissipated in the corona (*i.e.* $f = 0$). The dashed blue lines show how this anticorrelation is expected to vary as f increases (from left to right: $f = 0.4, 0.7, 0.9, 0.99$). Allowing for a reasonable range in f across different systems, the data show a good overall agreement with the Svensson & Zdziarski (1994) model.

wavelength of 4392 Å for which the above relation is calibrated. We calculate $\dot{M}$ using the 5100 Å luminosity reported by Peterson et al. (2004) here, as this is closer in wavelength to 4392 Å than the UVM2 band used for PG 1426+015 in Jiang et al. (2019a). [10] This combination gives $\log[m_{\rm BH}\dot{m}^2] = 6.18^{+0.56}_{-0.44}$.

The ensemble of AGN constraints shown in Fig. 12 are broadly consistent with the anticorrelation expected in the $\log[n_e/\mathrm{cm}^{-3}]$ versus $\log[m_{\rm BH}\dot{m}^2]$ plane based on the Svensson & Zdziarski (1994) model, though there is significant scatter (potentially related to different AGN exhibiting different values of f; Mallick et al. 2025). Although the relatively large density inferred for PG 1426+015 may initially seem surprising given its large mass, it actually sits comfortably within the scatter seen from other AGN in this plane.

[10]We also note that Jiang et al. (2019a) did not properly account for the frequency term included in equation (1), the impact of which is most significant for the small number of sources where UV bands were used to estimate $\dot{M}$ in that work. Use of the UV bands without making this correction, as was the case for PG 1426+015, significantly overpredicts $\dot{m}$, and thus the product $m_{\rm BH}\dot{m}^2$.

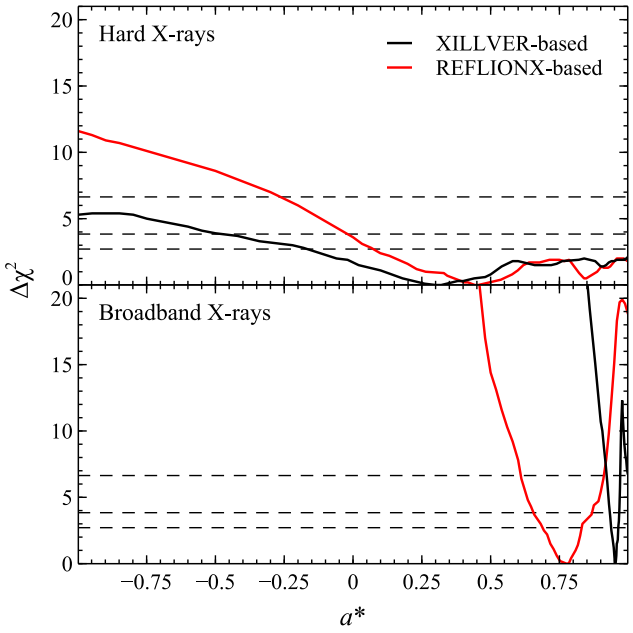

Figure 13. Top panel: the confidence contours for the black hole spin for PG 1426+015 obtained with the best-fit XILLVER-based (black) and REFLIONX-based reflection models obtained when considering the hard X-ray data only (>2 keV in the rest-frame of the source). The horizontal dashed lines represent the $\Delta\chi^2$ corresponding to the 90, 95, and 99 per cent confidence intervals. Bottom panel: as above, but for the best-fitting models obtained when fitting the full broad-band data set. In this case, we show the results for the models that adopt a phenomenological broken power-law emissivity profile, and the XILLVER-based model is the variant in which the O VIII flux is allowed to vary.

PG 1426+015 is therefore also broadly consistent with the same overall anti-correlation between $\log[n_e/\mathrm{cm}^{-3}]$ and $\log[m_{\rm BH}\dot{m}^2]$, and thus the general prediction of Svensson & Zdziarski (1994).

4.3 Black hole spin

The large mass of the black hole in PG 1426+015 makes it a key target for expanding the sample of AGN spin measurements. The mass–spin plane is a key diagnostic for SMBH growth models (*e.g.* Sesana et al. 2014; Bustamante & Springel 2019; Beckmann et al. 2024), and high-mass systems ($\log[m_{\rm BH}] \gtrsim 9$) carry particular diagnostic power (Piotrowska et al. 2024), since most models predict that more moderate mass systems ($\log[m_{\rm BH}] \sim 6-8$) should mostly be rapidly rotating. While there are a growing number of systems with both mass and spin constrained independently, such that the mass–spin plane is becoming increasingly populated, the majority of these SMBHs lie in the $\log[m_{\rm BH}] \sim 6-8$ range (Reynolds 2021), and the high-mass regime remains sparsely populated with just two constraints in the $\log[m_{\rm BH}] \geq 9$ range (Reynolds et al. 2014; Sisk-Reynés et al. 2022).

For both of the reflection models considered here (REFLIONX, XILLVER), the best-fitting models for the full broadband *XMM–Newton* + *NuSTAR* data set (the models involving a broken power-law emissivity profile, and additionally a variable O VIII line strength in the case of XILLVER) both provide constraints on the spin. However, the best-fitting XILLVER-based model prefers a higher spin ($a^* = 0.95 \pm 0.01$ at 90 per cent confidence; see Table 4) than the best-fitting REFLIONX-based model ($a^* = 0.77^{+0.06}_{-0.08}$; see Table 3); the confidence contours for both models are shown in Fig. 13. A

qualitatively similar difference can be seen when comparing the lamppost variants as well. As discussed in Madathil-Pottayil et al. (2024), this is because the XILLVER reflection model still typically has a weaker soft X-ray continuum than REFLIONX even for the same density parameter and, as such, the relative contribution of the emission lines to the overall soft X-ray flux in the reflection spectrum is larger for the XILLVER model. This means the XILLVER model requires stronger relativistic blurring than REFLIONX in order to produce the smooth soft excess seen in the data, requiring in turn a higher spin parameter or a steeper emissivity profile (or both).

Despite the above, the 3σ confidence intervals ($\Delta\chi^2 = 9$) for the best-fitting REFLIONX-based and XILLVER-based models do actually have some degree of overlap though. Furthermore, the difference in the two spin constraints is of a broadly similar magnitude to the systematic errors expected to be relevant for spin measurements ($\Delta a^* \sim 0.1$ for moderate-to-high spins) based on both parameter recovery simulations relating to spectral modelling (*e.g.* Bonson & Gallo 2016; Choudhury et al. 2017; Kammoun et al. 2018) and simulations exploring how robust the assumption that the disc truncates at the ISCO really is (Reynolds & Fabian 2008). The level of disagreement between the two models may therefore not be as severe as it first seems. Considering the parameter constraints from both models, one may conclude that reflection models for PG 1426+015 imply the spin of the central supermassive black hole is at least moderately high ($a^* \gtrsim 0.7$) when the full broadband data set is analysed.

It is important to stress, though, that even this combined constraint on the spin should still be considered model dependent in a more fundamental sense since it is clearly driven by the assumption that the soft excess is dominated by relativistic reflection; as discussed above, alternative models are frequently discussed in the literature (most notably the warm corona model). The high-energy data ($\gtrsim$2 keV), where the contribution from relativistic reflection is much less contentious, do not have sufficient S/N to meaningfully corroborate the broad-band constraints by themselves, and only provide very weak constraints on the spin, permitting essentially all positive values of a^* (i.e. prograde spins) for both of the reflection models considered; confidence contours for the fits that are based on only the hard X-ray band (Section 3.3) are also shown in Fig. 13. Again combining the constraints, the hard X-ray data can only limit the spin to $a^* \gtrsim -0.15$. The spin constraint for presented by Mallick et al. (2025) – who treat the soft excess with the warm corona model for PG 1426+015–is also similarly loose, allowing for the majority of the prograde parameter space ($0.3 \leq a^* \leq 0.93$). As such, the tighter constraints implied by the broadband modelling presented here may still need to be treated with caution.

5 CONCLUSIONS

We have presented the first broadband (*XMM–Newton* + *NuSTAR*) observation of the quasar PG 1426+015, which is powered by the black hole with the largest reverberation-mapped mass to date: $\log[M_{\rm BH}/M_{\odot}] = 9.01^{+0.11}_{-0.16}$. The *XMM–Newton* data, and in particular the high-resolution RGS spectrum, confirms that this source is another example of the rare subset of bare AGN. The broad-band spectrum shows a strong soft excess, as well as independent evidence for reflection from the innermost accretion disc via the presence of a relativistically broadened iron emission line and a clear Compton hump.

We use both XILLVER-based and REFLIONX-based models that allow the density of the disc to be a free parameter to test whether the soft excess in PG 1426+015 can be explained with relativistic reflection. Ultimately, we find that both reflection models are able to do so, but in the case of the XILLVER-based models considered we also find that the strength of the oxygen emission plays a key role in determining whether this is the case or not. XILLVER-based models with the level of oxygen emission included as standard struggle to fit the broad-band data, leaving clear hard excesses in the residuals (similar to the results found by some previous authors for other bare AGN), while XILLVER-based models that allow for a reduced amount of oxygen emission can fit the broad-band data well. In contrast, the REFLIONX-based models can fit the soft excess without the need for any such modification. Understanding this issue further will likely be key for determining whether relativistic reflection remains a viable explanation for the soft excess in general.

The reflection models that do fit the broad-band data well imply a high density for the accretion disc of $\log[n_{\rm e}/{\rm cm}^{-3}] \sim 18$, though PG 1426+015 is consistent with the loose anti-correlation between $\log[n_{\rm e}/{\rm cm}^{-3}]$ and $\log[m_{\rm BH}\dot{m}^2]$ seen from other AGN with reflection-based density constraints. These broad-band fits also provide preliminary constraints on the spin, in combination implying a moderate-to-high spin of $a^* \gtrsim 0.7$, though here there is formally a bit more tension between the two reflection models (with our best-fit REFLIONX model implying $a^* = 0.77^{+0.06}_{-0.08}$ and our best-fitting XILLVER model implying $a^* = 0.95 \pm 0.01$). This result is highly model dependent, though, as it relies on the soft excess being dominated by relativistic reflection; the hard X-ray data do not have sufficient S/N to provide a meaningful independent constraint from the iron line and Compton hump alone (only implying $a^* \gtrsim -0.15$). Further deep observations will be required to provide a less model-dependent constraint, but may be worthwhile given that its high black hole mass places PG 1426+015 in a sparsely populated part of the spin–mass plane for SMBHs.

ACKNOWLEDGEMENTS

The authors would like to thank the reviewer for their positive feedback, which helped to improve the final version of the manuscript. DJW acknowledges support from the Science and Technology Facilities Council (STFC; grant code ST/Y001060/1). PK acknowledges support from the National Aeronautics and Space Administration (NASA) through the NASA Hubble Fellowship grant HST-HF2-51534.001-A awarded by the Space Telescope Science Institute, which is operated by the Association of Universities for Research in Astronomy, Incorporated, under NASA contract NAS5-26555. CP is supported by PRIN MUR SEAWIND–European Union–NextGenerationEU. This research has made use of data obtained with *NuSTAR*, a project led by Caltech, funded by NASA and managed by the NASA Jet Propulsion Laboratory (JPL), and has utilized the NUSTARDAS software package, jointly developed by the Space Science Data Centre (SSDC; Italy) and Caltech (USA). This research has also made use of data obtained with *XMM–Newton*, an ESA science mission with instruments and contributions directly funded by European Space Agency (ESA) Member States.

DATA AVAILABILITY

All of the raw data used in this article are publicly available from ESA's *XMM–Newton* Science Archive[11] and NASA's HEASARC archive.[12]

[11] https://www.cosmos.esa.int/web/xmm-newton/xsa
[12] https://heasarc.gsfc.nasa.gov/

REFERENCES

Alston W. N. et al., 2020, Nat. Astron., 4, 597
Anders E., Grevesse N., 1989, Geochim. Cosmochim. Acta, 53, 197
Antonucci R., 1993, ARA&A, 31, 473
Arnaud K. A., 1996, in Jacoby G. H., Barnes J., eds, ASP Conf. Ser., Vol. 101, Astronomical Data Analysis Software and Systems V. Astron. Soc. Pac., San Francisco, p. 17
Arnaud K. A. et al., 1985, MNRAS, 217, 105
Baloković M. et al., 2018, ApJ, 854, 42
Bambi C. et al., 2021, Space Sci. Rev., 217, 65
Bardeen J. M., Press W. H., Teukolsky S. A., 1972, ApJ, 178, 347
Beckmann R. S. et al., 2024, MNRAS, 527, 10867
Bentz M. C., Katz S., 2015, PASP, 127, 67
Bianchi S., Guainazzi M., Matt G., Fonseca Bonilla N., 2007, A&A, 467, L19
Bianchi S., Guainazzi M., Matt G., Fonseca Bonilla N., Ponti G., 2009, A&A, 495, 421
Bonson K., Gallo L. C., 2016, MNRAS, 458, 1927
Brenneman L. W., Reynolds C. S., 2006, ApJ, 652, 1028
Brightman M. et al., 2013, MNRAS, 433, 2485
Bustamante S., Springel V., 2019, MNRAS, 490, 4133
Cackett E. M., Fabian A. C., Zogbhi A., Kara E., Reynolds C., Uttley P., 2013, ApJ, 764, L9
Cash W., 1979, ApJ, 228, 939
Choudhury K., García J. A., Steiner J. F., Bambi C., 2017, ApJ, 851, 57
Crummy J., Fabian A. C., Gallo L., Ross R. R., 2006, MNRAS, 365, 1067
Dauser T., García J., Walton D. J., Eikmann W., Kallman T., McClintock J., Wilms J., 2016, A&A, 590, A76
Dauser T. et al., 2022, MNRAS, 514, 3965
Dauser T., Wilms J., Reynolds C. S., Brenneman L. W., 2010, MNRAS, 409, 1534
De Marco B. et al., 2013, MNRAS, 431, 2441
den Herder J. W. et al., 2001, A&A, 365, L7
Done C., Davis S. W., Jin C., Blaes O., Ward M., 2012, MNRAS, 420, 1848
Fabian A. C., Rees M. J., Stella L., White N. E., 1989, MNRAS, 238, 729
Fabian A. C. et al., 2009, Nat, 459, 540
García J. et al., 2014, ApJ, 782, 76
García J., Kallman T. R., 2010, ApJ, 718, 695
García J. A. et al., 2016, MNRAS, 462, 751
García J. A. et al., 2019, ApJ, 871, 88
García J. A. et al., 2020, ApJ, 897, 67
George I. M., Fabian A. C., 1991, MNRAS, 249, 352
Gierliński M., Done C., 2004, MNRAS, 349, L7
Gonzalez A. G., Wilkins D. R., Gallo L. C., 2017, MNRAS, 472, 1932
Grevesse N., Sauval A. J., 1998, Space Sci. Rev., 85, 161
Harrison F. A. et al., 2013, ApJ, 770, 103
HI4PI Collaboration et al., 2016, A&A, 594, A116
Jansen F. et al., 2001, A&A, 365, L1
Jiang J., Dauser T., Fabian A. C., Alston W. N., Gallo L. C., Parker M. L., Reynolds C. S., 2022, MNRAS, 514, 1107
Jiang J. et al., 2018, MNRAS, 477, 3711
Jiang J. et al., 2019a, MNRAS, 489, 3436
Jiang J., Walton D. J., Fabian A. C., Parker M. L., 2019b, MNRAS, 483, 2958
Kallman T., Bautista M., 2001, ApJS, 133, 221
Kammoun E. S., Nardini E., Risaliti G., 2018, A&A, 614, A44
Kaspi S., Smith P. S., Netzer H., Maoz D., Jannuzi B. T., Giveon U., 2000, ApJ, 533, 631
Kosec P., Zoghbi A., Walton D. J., Pinto C., Fabian A. C., Parker M. L., Reynolds C. S., 2020, MNRAS, 495, 4769
Laha S., Guainazzi M., Dewangan G. C., Chakravorty S., Kembhavi A. K., 2014, MNRAS, 441, 2613
Laor A., 1991, ApJ, 376, 90
Madathil-Pottayil A. et al., 2024, MNRAS, 534, 608
Madsen K. K., Grefenstette B. W., Pike S., Miyasaka H., Brightman M., Forster K., Harrison Fiona A., 2020, preprint (arXiv:2005.00569)
Magdziarz P., Zdziarski A. A., 1995, MNRAS, 273, 837
Mallick L. et al., 2018, MNRAS, 479, 615
Mallick L. et al., 2022, MNRAS, 513, 4361
Mallick L. et al., 2025, preprint (arXiv:2501.15380)
Martocchia A., Karas V., Matt G., 2000, MNRAS, 312, 817
Matt G. et al., 2014, MNRAS, 439, 3016
Mehdipour M. et al., 2015, A&A, 575, A22
Middei R. et al., 2020, A&A, 640, A99
Miniutti G., Ponti G., Greene J. E., Ho L. C., Fabian A. C., Iwasawa K., 2009, MNRAS, 394, 443
Morrison R., McCammon D., 1983, ApJ, 270, 119
Page K. L., Schartel N., Turner M. J. L., O'Brien P. T., 2004, MNRAS, 352, 523
Peterson B. M. et al., 2004, ApJ, 613, 682
Petrucci P. O. et al., 2020, A&A, 634, A85
Petrucci P. O. et al., 2018, A&A, 611, A59
Piotrowska J. M. et al., 2024, Front. Astron. Space Sci., 11, 1324796
Porquet D., Reeves J. N., Hagen S., Lobban A., Braito V., Grosso N., Marin F., 2024, A&A, 689, A336
Porquet D. et al., 2018, A&A, 609, A42
Porquet D., Reeves J. N., O'Brien P., Brinkmann W., 2004, A&A, 422, 85
Raimundo S. I., Fabian A. C., Vasudevan R. V., Gand hi P., Wu J., 2012, MNRAS, 419, 2529
Reynolds C. S., 2021, ARA&A, 59, 117
Reynolds C. S., Begelman M. C., 1997, ApJ, 488, 109
Reynolds C. S., Fabian A. C., 2008, ApJ, 675, 1048
Reynolds M. T., Walton D. J., Miller J. M., Reis R. C., 2014, ApJ, 792, L19
Ricci C. et al., 2017, ApJS, 233, 17
Risaliti G. et al., 2013, Nat, 494, 449
Ross R. R., Fabian A. C., 2005, MNRAS, 358, 211
Rózańska A., Malzac J., Belmont R., Czerny B., Petrucci P. O., 2015, A&A, 580, A77
Sesana A., Barausse E., Dotti M., Rossi E. M., 2014, ApJ, 794, 104
Sisk-Reynés J., Reynolds C. S., Matthews J. H., Smith R. N., 2022, MNRAS, 514, 2568
Strüder L. et al., 2001, A&A, 365, L18
Svensson R., Zdziarski A. A., 1994, ApJ, 436, 599
Turner M. J. L. et al., 2001, A&A, 365, L27
Ursini F., Dovčiak M., Zhang W., Matt G., Petrucci P. O., Done C., 2020a, A&A, 644, A132
Ursini F. et al., 2020b, A&A, 634, A92
Vaughan S., Fabian A. C., Ballantyne D. R., De Rosa A., Piro L., Matt G., 2004, MNRAS, 351, 193
Verner D. A., Ferland G. J., Korista K. T., Yakovlev D. G., 1996, ApJ, 465, 487
Walton D. J. et al., 2020, MNRAS, 499, 1480
Walton D. J. et al., 2021, MNRAS, 506, 1557
Walton D. J. et al., 2018, MNRAS, 473, 4377
Walton D. J., Nardini E., Fabian A. C., Gallo L. C., Reis R. C., 2013, MNRAS, 428, 2901
Walton D. J., Reynolds M. T., Miller J. M., Reis R. C., Stern D., Harrison F. A., 2015, ApJ, 805, 161
Walton D. J., Reynolds M. T., Stern D., Brightman M., Lemon C., 2022, MNRAS, 516, 5997
Walton D. J. et al., 2014, ApJ, 788, 76
Walton D. J. et al., 2016, ApJ, 826, 87
Wilkins D. R., Fabian A. C., 2012, MNRAS, 424, 1284
Wilkins D. R., Gallo L. C., Costantini E., Brandt W. N., Blandford R. D., 2022, MNRAS, 512, 761
Wilms J., Allen A., McCray R., 2000, ApJ, 542, 914
Xiang X. et al., 2022, MNRAS, 515, 353
Xu Y., García J. A., Walton D. J., Connors R. M. T., Madsen K., Harrison F. A., 2021, ApJ, 913, 13
Zdziarski A. A., Johnson W. N., Magdziarz P., 1996, MNRAS, 283, 193
Zycki P. T., Done C., Smith D. A., 1999, MNRAS, 309, 561

This paper has been typeset from a TEX/LATEX file prepared by the author.